

Probing transport and slow relaxation in the mass-imbalanced Fermi-Hubbard model

N. Darkwah Oppong,^{1,2,3,*} G. Pasqualetti,^{1,2,3} O. Bettermann,^{1,2,3}
 P. Zechmann,^{4,3} M. Knap,^{4,3} I. Bloch,^{1,2,3} and S. Fölling^{1,2,3}

¹Ludwig-Maximilians-Universität, Schellingstraße 4, 80799 München, Germany

²Max-Planck-Institut für Quantenoptik, Hans-Kopfermann-Straße 1, 85748 Garching, Germany

³Munich Center for Quantum Science and Technology (MCQST), Schellingstraße 4, 80799 München, Germany

⁴Department of Physics and Institute for Advanced Study,
 Technical University of Munich, 85748 Garching, Germany

(Dated: November 26, 2020)

Constraints in the dynamics of quantum many-body systems can dramatically alter transport properties and relaxation time scales even in the absence of static disorder. Here, we report on the observation of such constrained dynamics arising from the distinct mobility of two species in the one-dimensional mass-imbalanced Fermi-Hubbard model, realized with ultracold ytterbium atoms in a state-dependent optical lattice. By displacing the trap potential and monitoring the dynamical response of the system, we identify suppressed transport and slow relaxation with a strong dependence on the mass imbalance and interspecies interaction strength, suggesting eventual thermalization for long times. Our observations are supported by numerical simulations and pave the way to study metastability arising from dynamical constraints in other quantum many-body systems.

I. INTRODUCTION

The fundamental understanding of thermalization and its failure in isolated quantum many-body systems has seen remarkable progress in recent years, driven both by novel theoretical concepts [1–4] and emerging experimental platforms for quantum simulations such as ultracold atoms, trapped ions, and superconducting qubits [5–7]. The simplest approach to the problem is to posit the two distinct classes of ergodic and non-ergodic dynamics. In the former case, fast relaxation to a local equilibrium is followed by slow thermalization of globally conserved quantities according to the laws of hydrodynamics [8–11]. By contrast, non-ergodic dynamics can arise in systems with a large number of conserved quantities, as exemplified by many-body localization in strongly disordered quantum systems [12–15] that retain their memory of an initial state for arbitrarily long times [16–18].

Recent experimental and theoretical investigations of non-equilibrium dynamics in isolated quantum many-body systems, however, suggest considerable refinements to this classification. For instance, Rydberg quantum simulators have observed surprising oscillatory dynamics in the blockade regime [19, 20], and the slow late-time dynamics of fractonic quantum matter with constrained excitations [21] is described by substantially modified hydrodynamic equations [22–25]. Furthermore, interacting mixtures of heavy and light particles [see Fig. 1(a)] have even been proposed to feature a dynamical type of many-body localization arising from the heavy particles acting as a form of disorder for the light ones [26–29]. Although subsequent studies have suggested that such heavy-light mixtures are ergodic and do thermalize at late times, the relaxation of initial non-equilibrium states is expected to be extremely slow with an emergence of

metastability [30–33]. This is a direct consequence of the strongly constrained motion in the presence of mass imbalance and interactions. However, since such heavy-light mixtures are particularly challenging to simulate with classical resources, these theoretical studies do not

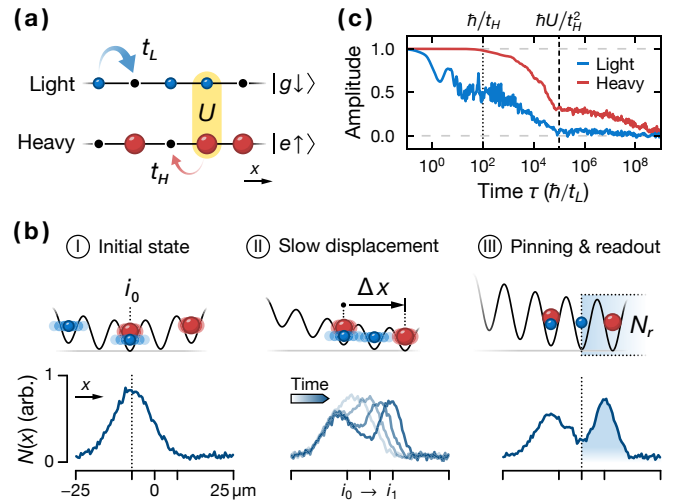


FIG. 1. Transport in the mass-imbalanced Fermi-Hubbard model. (a) Illustration of the mass-imbalanced Fermi-Hubbard model with on-site interaction U and hopping $t_L \gg t_H$ of the light (blue circles) and heavy (red circles) particles, respectively. We also show the atomic states relevant for the experimental implementation. (b) Schematic representation of the different steps in our transport measurement (top row) and integrated densities of the light atoms (bottom row) from experimental snapshots. (c) Decay of the amplitude of an initial long-wavelength density modulation in a small homogeneous system with eight lattice sites, periodic boundary conditions, four particles of each species, $t_H/t_L = 0.01$, and $U/t_L = 10$.

entirely agree on the exact properties of relaxation [31–33], which underlines the importance of experimental evidence. Crucially, this phenomenology connects to the general question of how dynamical constraints can introduce slow equilibration and non-ergodicity in quantum many-body systems [34–37].

In this work, we experimentally study the non-equilibrium dynamics of a heavy-light mixture with an ultracold quantum gas of ^{171}Yb atoms in an optical lattice. Our experiment realizes the strongly mass-imbalanced Fermi-Hubbard model in one dimension (1D), as illustrated in Fig. 1(a). In addition to the $^1\text{S}_0$ ground state (denoted $|g\rangle$), the alkaline-earth-like atom ^{171}Yb features the metastable $^3\text{P}_0$ excited state (denoted $|e\rangle$), often referred to as clock state [38]. We harness a state-dependent optical lattice (SDL) [39] to introduce different time scales for the hopping of atoms in $|g\rangle$ and $|e\rangle$ taking on the role of light and heavy particles, respectively. Our system is harmonically confined, and we gradually displace the trap minimum with the help of an additional optical potential to probe the transport dynamics of the light species [see Fig. 1(b)]. Measuring the dynamics of the atomic cloud, we find relaxation at late times as a signature of ergodicity for all finite interaction parameters. For strong interactions and large mass imbalance, this relaxation is extremely slow as expected for the onset of a metastable regime. Our experimental results can be understood as emergent properties from the constrained many-body dynamics and are supported by numerical simulations based on matrix product states and exact diagonalization.

II. EXPERIMENT

Our experiment begins with a Fermi gas of ^{171}Yb atoms in a balanced mixture of the two nuclear spins $|m_F = -1/2\rangle \equiv |\downarrow\rangle$ and $|m_F = +1/2\rangle \equiv |\uparrow\rangle$ in the ground state $|g\rangle$. In the initial optical dipole trap, we prepare a total of $\approx 10^4$ atoms at a temperature of $T \simeq 0.15T_F$ with T_F the Fermi temperature. The weakly-interacting spin mixture is loaded from the optical dipole trap into the ground band of a two-axes $\approx 30E_{\text{rec}}^m$ deep state-independent lattice operated at the magic wavelength ($\lambda_m = 759.3\text{ nm}$) [40] and a $V_L = 6.9(3)E_{\text{rec}}$ deep SDL ($\lambda = 671.5\text{ nm}$) along the third axis. Here, $E_{\text{rec}}^m = h \times 2.0\text{ kHz}$ and $E_{\text{rec}} = h \times 2.6\text{ kHz}$ are the recoil energies of the corresponding lattice photons. The atoms are non-uniformly distributed across the array of decoupled 1D systems (tubes) generated by the perpendicular state-independent lattices. We estimate ≈ 300 tubes are considerably filled with a mean atom number of $\mathcal{N} \simeq 18$ per spin state and standard deviation $\Delta\mathcal{N} \simeq 8$. In a typical tube, the atoms are spread over a system size of $l \approx 30$ lattice sites (root-mean-square width) [41].

Shortly after loading the lattices, we use a 0.17 ms long

clock laser pulse to selectively drive atoms from $|g \uparrow\rangle$ to $|e \uparrow\rangle$. This suddenly introduces a distinct hopping amplitude $t_H \simeq h \times 5\text{ Hz} \ll t_L$ for the clock state atoms in $|e \uparrow\rangle \equiv |H\rangle$ (heavy). Here, $t_L \simeq h \times 105\text{ Hz}$ is the unaltered hopping amplitude of the remaining ground state atoms in $|g \downarrow\rangle \equiv |L\rangle$ (light). The ratio of the hopping amplitudes and the associated mass imbalance is determined by the different lattice depths V_L and $V_H = 3.06(4)V_L$ experienced by $|L\rangle$ and $|H\rangle$ atoms in the SDL [41]. We ensure that the mixture initially remains non-interacting by ramping the magnetic field to the zero crossing of an orbital Feshbach resonance at $\simeq 1533\text{ G}$ [41, 42] before the excitation pulse. Finally, we lower the SDL depth to adjust the hopping ratio t_H/t_L and slowly ramp the magnetic field to 1400-1600 G in accordance with the desired interaction strength. We note that the fraction of doublons as a critical property of the initial state only weakly depends on the chosen interaction parameter [41]. After the state preparation procedure, we translate the minimum of the trapping potential along the tubes by slowly turning on a displaced, state-independent dipole trap, which initiates the transport dynamics. Following the subsequent evolution, we rapidly ramp up the SDL to $V_L \approx 15E_{\text{rec}}$, which freezes the motion of light and heavy atoms. We then turn off the magnetic field and record the density of the light atoms with in-situ absorption imaging and determine the fraction transported to the new trap minimum [see Fig. 1(b)]. Our imaging intrinsically integrates along one axis of the system, which averages the measurement over an ensemble of tubes with different atom numbers [41].

III. MODEL

Each tube in our experiment is described by a 1D Fermi-Hubbard model with mass imbalance,

$$\hat{\mathcal{H}} = - \sum_{i,\alpha \in \{L,H\}} t_\alpha \left[\hat{c}_{i\alpha}^\dagger \hat{c}_{(i+1)\alpha} + \text{h.c.} \right] + U \sum_i \hat{n}_{iL} \hat{n}_{iH} + \frac{\kappa}{2} \sum_{i,\alpha \in \{L,H\}} (i - i_0)^2 \hat{n}_{i\alpha}. \quad (1)$$

Here, $\hat{c}_{i\alpha}$ ($\hat{c}_{i\alpha}^\dagger$) denotes the fermionic creation (annihilation) operator for a light ($\alpha = L$) or heavy ($\alpha = H$) atom, $\hat{n}_{i\alpha} \equiv \hat{c}_{i\alpha}^\dagger \hat{c}_{i\alpha}$ the corresponding number operator, t_α the hopping amplitude of each species, and U the on-site interaction. The harmonic confinement is determined by the trap minimum i_0 and strength $\kappa = m\omega^2 d^2 = h \times 3.1(1)\text{ Hz}$ with the atomic mass m , trapping frequency $\omega = 2\pi \times 40(1)\text{ Hz}$, and lattice spacing $d = \lambda/2$. Here, we are interested in the regime $t_L \gg t_H$, where the model is expected to feature extremely slow relaxation. In Fig. 1(c), we show numerical results from exact diagonalization for the decay of an initial long-wavelength density modulation of both species

in a homogeneous system ($\kappa = 0$) for small hopping ratio $t_H/t_L = 0.01$ and strong interactions $U/t_L = 10$, evaluated at infinite temperature. In agreement with previous results [32], we identify a separation of time scales with a metastable regime at short times $\lesssim \hbar/t_H$. Beyond this natural time scale of the heavy species, slow relaxation sets in until $\sim \hbar U/t_H^2$ [see Fig. 1(c)], when the system enters another metastable regime with even slower dynamics. This emergent time scale can be attributed to bound states comprised of two heavy particles on neighboring lattice sites and a light particle delocalized over these sites. For $U \gg t_L \gg t_H$, such configurations move collectively, which introduces a transport bottleneck on time scales $\sim \hbar U/t_H^2$ [28]. In addition, bound states with a larger number of neighboring heavy atoms can occur—albeit less frequently—in the thermal average over different Fock states, causing a hierarchy in the decay of the amplitude. In the following measurements, we focus on the parameter regime $t_H/t_L \gtrsim 0.1$ and $|U|/t_L \lesssim 10$ in order to characterize the dynamics over the relevant time scales, which would otherwise be outside of experimentally accessible observation times [41].

IV. LOCALIZED SINGLE-PARTICLE STATES

In a first reference measurement, we characterize the single-particle physics originating from the harmonic confinement $\kappa > 0$ in our experiment. It gives rise to single-particle localized eigenstates at the edge of the trap, a phenomenon studied in Refs. [43–47]. These Stark-localized states occur due to the finite gradient $\partial_i \hat{\mathcal{H}} = \kappa(i - i_0)\hat{n}_{i\alpha}$ between neighboring lattice sites [48]. To experimentally probe this effect, we prepare a clean sample of non-interacting light atoms by employing a short resonant “push” pulse that removes all $|g \uparrow\rangle$ atoms. Subsequently, we measure the response to a linear translation of the trap minimum as shown in Fig. 1(b). Here, the trap minimum is displaced by $\Delta x/d = i_1 - i_0 = 47(3)$ within time $90(5)\hbar/t_L$ and we consider variable κ/t_L by adjusting the SDL depth in the range $0.69(3)$ – $11.8(5)E_{\text{rec}}$.

For all finite lattice depths, we observe a separation of the atoms into two clouds, one close to the initial trap minimum i_0 and one at the final trap minimum i_1 , as visible in the insets of Fig. 2(a). We quantify this by determining the number of atoms in the right half of the system N_r , which corresponds to $i \geq i_0 + \Delta x/(2d)$, and compare it to the total number of atoms N . When measuring N_r before the displacement of the trap minimum, we find a nearly constant value of $\approx 10\%$, which we attribute to our finite imaging resolution and a small extent of the initial cloud into the counting region. In Fig. 2(a), we plot the fraction of transported atoms, N_r/N , which is exponentially suppressed for increasing confinement strength. This significant reduction of mass transport in the system can be explained with the properties of the single-particle

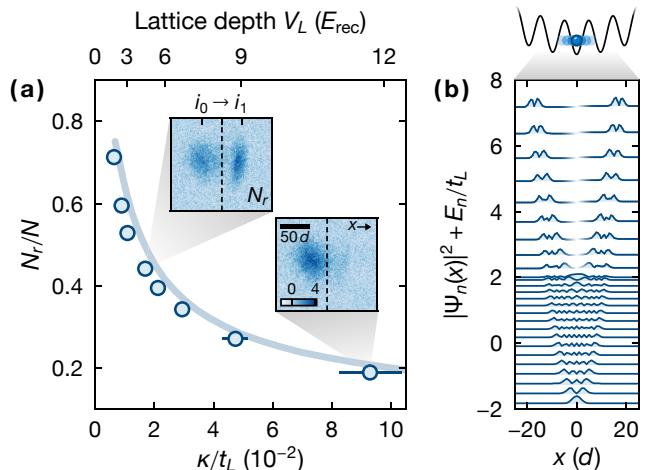


FIG. 2. Stark localization in the absence of interactions. (a) Fraction of light atoms N_r/N transported to the right half of the system (blue circles) in the absence of heavy atoms and for variable confinement κ/t_L determined by the lattice depth V_L . Each point is the average of 2-5 measurements, and error bars indicate the uncertainty of κ/t_L (partly smaller than the marker size). The solid line corresponds to a theoretical calculation [41], and the insets show raw atomic column densities for $\kappa/t_L = 1.7(1) \times 10^{-2}$ and $9(1) \times 10^{-2}$ with the dashed lines indicating the boundary that determines the atom count N_r in the right half of the system. (b) Probability density $|\Psi_n(x)|^2$ and eigenenergy E_n/t_L of the lowest-lying single-particle eigenstates for $V_L = 9E_{\text{rec}}$ ($\kappa/t_L = 4.9 \times 10^{-2}$). We add a small linear potential to lift the degeneracy of the localized states.

eigenstates, which are visualized in Fig. 2(b). In general, eigenstates with energies $E_n \in [-2t_L, 2t_L]$ are delocalized across the trap with a non-zero probability density at the center. This behavior changes dramatically for energies $E_n > 2t_L$ corresponding to localized states, in which atoms cannot efficiently follow the displaced trap minimum. Crucially, the number of states with $E_n \leq 2t_L$ is reduced as we increase κ/t_L and therefore, a larger number of localized states becomes occupied in each tube. This explains the observed suppression of N_r/N , which we also reproduce with a theoretical calculation [41] of the experimental protocol [see Fig. 2(a)].

V. INHIBITED TRANSPORT AT EARLY TIMES

Next, we probe how interactions with the heavy species modify the mobility of the light atoms. For this measurement, we set the interaction strength $U/t_L \in [-20, 5]$, a range accessible via magnetic field tuning of the orbital Feshbach resonance, and choose the fixed hopping ratio $t_H/t_L \simeq 0.1$ and confinement $\kappa/t_L \simeq 1.7 \times 10^{-2}$ by ramping the SDL to $4.7(2)E_{\text{rec}}$. Here, the confinement $\kappa/t_H \simeq 10\kappa/t_L = 1.7 \times 10^{-1}$ suggests that most heavy atoms occupy single-particle localized states according to our

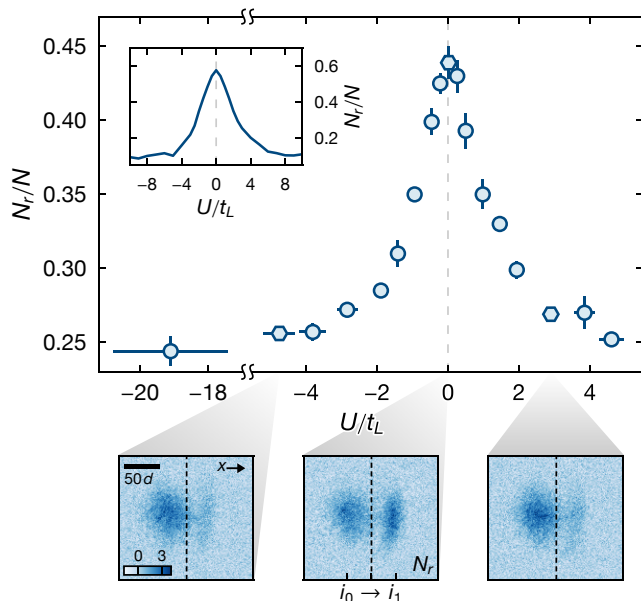


FIG. 3. Constrained early-time dynamics in the interacting heavy-light mixture. Fraction of light atoms N_r/N transported to the right half of the system (blue markers) for variable heavy-light interaction strength U , fixed hopping ratio $t_H/t_L = 0.104(7)$, and confinement $\kappa/t_L = 1.7(1) \times 10^{-2}$. Each point is the average of 3-4 measurements, and error bars (partly smaller than the marker size) denote the standard error of the mean of N_r/N and the uncertainty of U/t_L . The bottom panels show raw atomic column densities for $U/t_L = -4.8(4)$, $0.02(4)$, and $2.9(2)$ (from left to right, hexagonal markers) with the dashed lines indicating the boundary that determines the atom count N_r in the right half of the system. The inset of the main panel, shows the numerical matrix-product state simulations of a single tube with the Hubbard parameters and confinement strength of the experiment and $\mathcal{N}_{\text{sim}} = 5$ atoms of each species.

previous measurement in the non-interacting regime [see Fig. 2(a)]. However, in the presence of interactions, several of these states delocalize in analogy to the suggested critical gradient required for localization of the interacting Stark ladder [44, 49–52]. We numerically verify this for our mass-imbalanced case and find a central trap region of ≈ 30 lattice sites, where the heavy atoms are mobile already at short times for finite but weak interaction strengths [41]. Thus, a significant fraction of the system will be responsive to the displacement of the trap potential.

In analogy to our first measurement, we again determine the fraction of transported atoms after displacing the trap minimum by $47(3)d$ within time $92(5)\hbar/t_L$. As we increase the interaction strength $|U|/t_L$, we find a substantial reduction of the transported fraction N_r/N up to a factor of two compared to $U = 0$ [see Fig. 3]. The behavior for attractive ($U < 0$) and repulsive ($U > 0$) interactions is almost identical, which we attribute to a similar initial state [41] and the dynamical symme-

try of our model in the limit $\kappa = 0$ [53]. We find the most significant change in the fraction of transported atoms to occur for interaction energies within the bandwidth $[-2t_L, 2t_L]$, whereas the signal saturates and remains nearly constant and at a low value for $|U|/t_L > 4$. To support our experimental data, we perform matrix-product state simulations for the Fermi-Hubbard model described in Eq. (1) and a simplified version of the experimental protocol [41]. As shown in the inset of Fig. 3, the extracted N_r/N curve agrees qualitatively with the experiment, and we attribute the quantitative disagreement to the significantly lower atom number in the simulation, $\mathcal{N}_{\text{sim}} = 5 < \mathcal{N}$.

In our measurement, the apparent suppression of transport results from the constraints in the dynamics of the light atoms arising due to interactions with the heavy species, as explored in Fig. 1(c). We emphasize that this measurement is an exclusive probe of the early time dynamics $\sim \hbar/t_H$ since the system is effectively frozen and fully separated towards the end of the gradual displacement over the relatively large distance $\Delta x/d \simeq 47$, which exceeds the typical system size $l \approx 30$ (see bottom panels of Fig. 3).

VI. SLOW RELAXATION AT LATE TIMES

We now turn to the dynamical response of the heavy-light mixture for later times, which we probe by systematically monitoring the in-situ density dynamics for variable hold time $\tau \in [0, 400\hbar/t_L]$ after translating the trap minimum. This allows us to observe the evolution of the non-equilibrium state directly. Here, we reduce the displacement to $\Delta x/d = 20(3) < l$ while keeping the speed $\approx 0.5d(t_L/\hbar)$ unchanged to ensure that the system remains connected and a significant fraction of the heavy atoms are mobile over the traversed distance. The relaxation dynamics can be captured by quantifying the change of the in-situ density distribution between the initial state after the translation of the trap minimum at $\tau = 0$ and later times. To this end, we introduce the density deviation observable,

$$\delta n(\tau) = \left\{ \int dx n(x, \tau) [n(x, \tau) - n(x, 0)]^2 \right\}^{(1/2)}, \quad (2)$$

which is obtained from the density of the light atoms integrated perpendicularly to the transport direction x and normalized such that $\int dx n(x, \tau) = 1$. For a slow relaxation of the density, this observable grows monotonously with increasing τ , whereas a constant $\delta n(\tau)$ indicates a stationary state of the system.

We probe the influence of the interaction strength and hopping ratio on the dynamics by measuring the density deviation for $t_H/t_L \simeq 0.2, 0.1$ and $U/t_L \simeq 0, -2, -10$, as shown in Fig. 4. For these parameters, the inte-

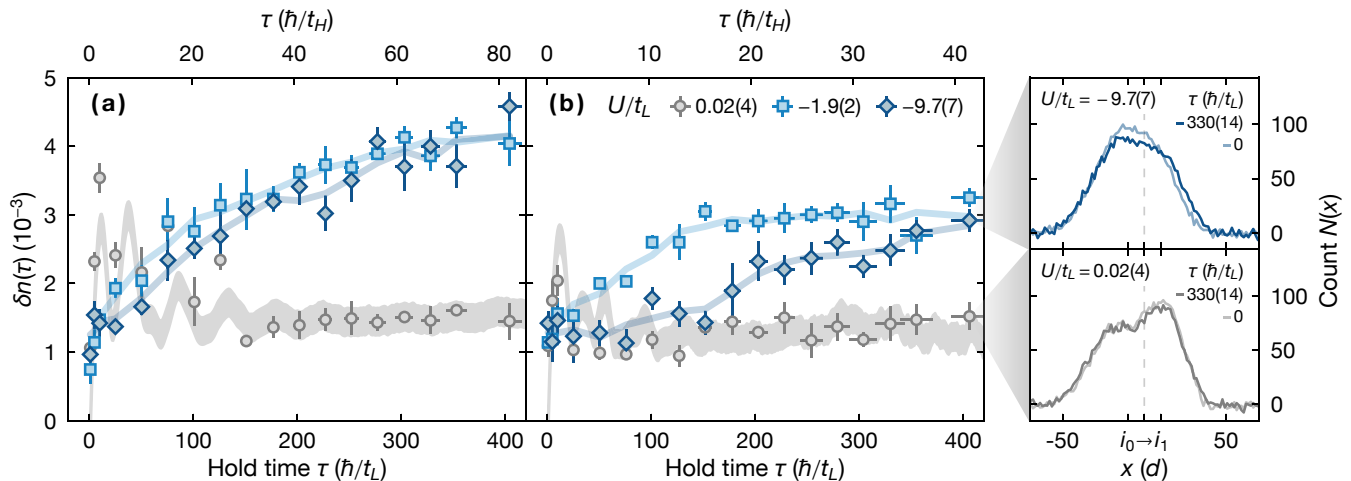


FIG. 4. Late-time relaxation dynamics. Density deviation $\delta n(\tau)$ of the light atoms with respect to the initial atom distribution after translating the trap minimum [see Eq. (2)], for variable hold time $\tau > 0$ and heavy-light interaction strength (see legend) with (a) $t_H/t_L = 0.203(8)$ and (b) $0.102(6)$. Each data point is calculated from the average of four atomic densities. Error bars (partly smaller than the marker size) denote the uncertainty of τ and standard error of $\delta n(\tau)$ from jackknife resampling [54]. The colored lines are three-point moving averages serving as a guide to the eye. We show a theoretical calculation for $U = 0$ as a gray band with the height derived from the estimated systematic uncertainty of $\delta n(\tau)$ [41]. The two right panels show integrated atomic densities, which are used to calculate $\delta n(\tau = 330\hbar/t_L)$ in panel (b).

grated atomic densities $n(x, \tau)$ show that the light atoms drift towards the final trap minimum at late times [see right panels of Fig. 4(b)]. First, we focus on the non-interacting time traces with $U/t_L \simeq 0$, which show oscillatory changes of $\delta n(\tau)$ at early times for both hopping ratios. These large-amplitude transients are quickly damped due to contributions from different eigenstates. For later times $\tau \gtrsim 100\hbar/t_L$, the density deviation reaches an almost stationary signal, which we also expect from our theoretical calculation.

For finite interaction strengths, we find a contrasting behavior with a strong dependence on the hopping ratio and interaction strength. In the following analysis, we focus on the comparison of time traces with the same hopping ratio, which contain a similar contribution from Stark-localized states at the edge of the atomic cloud. For $t_H/t_L \simeq 0.2$, the density deviation $\delta n(\tau)$ increases steadily and evolves similarly for both finite interaction strengths, with a slower relaxation for $U/t_L \simeq -10$ [see Fig. 4(a)]. To demonstrate that the slow relaxation results from dynamical constraints induced through mass-imbalance, we compare the decay time scales to numerical simulations for the mass-balanced Fermi-Hubbard model in a trap and interaction strength $U/t_L = -10$. In this case, we numerically estimate the time scale $\tau^* \approx 60\hbar/t_L$ for the decay of a long-wavelength modulation analogous to our transport measurement [41]. For the mass-imbalanced case of our experiment, we find the decay time $278(68)\hbar/t_L$, which is extracted from an exponential fit of the $U/t_L \simeq -10$ data in Fig. 4(a). This time

scale is significantly slower than τ^* , highlighting the relevance of the constrained dynamics in our measurement.

For the even smaller $t_H/t_L \simeq 0.1$, the data shows pronouncedly different features for the two finite interaction parameters [see Fig. 4(b)]. For $U/t_L \simeq -2$, the signal relaxes towards an apparently stationary value over the initial $200\hbar/t_L$. By contrast, for $U/t_L \simeq -10$, the density deviation first evolves into a plateau-like feature until $\tau \sim 150\hbar/t_L$, potentially indicating a regime of metastability where the light atoms remain immobile. For later times, the signal shows a continuously slow relaxation towards larger values. Our theoretical calculations for the experimental parameters suggest the onset of the second metastable regime [dashed line in Fig. 1(c)] at $\tau \approx 270\hbar/t_L$ [41], which appears to be consistent with the much slower relaxation observed experimentally for $\tau \gtrsim 250\hbar/t_L$.

Besides the closed system dynamics, according to Eq. (1), experimental imperfections could also drive the relaxation of $\delta n(\tau)$. Most notably, we expect the mobility of the light species to increase from the small loss of heavy atoms, which becomes appreciable for $\tau \gg 100\hbar/t_L$ and reaches up to $\approx 20\%$ at $\tau \simeq 400\hbar/t_L$ [41]. However, these losses should be mostly independent of U/t_L since the dominant dissipation process is the off-resonant scattering of SDL photons. By contrast, our data shows a strong interaction dependence. Thus, we conclude that the distinct features of the time traces cannot be solely caused by dissipation.

VII. DISCUSSION AND OUTLOOK

We have characterized the density dynamics of the mass-imbalanced Fermi-Hubbard model after a gradual change of the external trapping potential, which can be summarized as follows. First, increasing the interactions reduces the mobility of the light atoms significantly at short times. However, our data shows slow relaxation of the density for all finite interaction parameters and hopping ratios at late times. This strongly suggests that the central region of the system, which is unaffected by Stark localization, is indeed ergodic and thermalizes at late times—in agreement with theoretical studies of similar models [31–33, 55, 56]. Second, the observed relaxation time scales, even for intermediate hopping ratios $t_H/t_L \simeq 0.2$, are significantly longer than the decay time estimated for the mass-balanced case, which is a direct consequence of the dynamical constraints induced by the heavy species. Finally, for the strongest interaction $U/t_L \simeq -10$ and smallest hopping ratio $t_H/t_L \simeq 0.1$ probed in our experiment, the system relaxes extremely slowly with an overall time scale compatible with the expected emergence of a metastable regime. Thus, our experimental platform gives access to a particularly interesting class of dynamically constrained systems with a metastable regime that exists in the absence of static disorder and can be controlled solely by interactions.

In future experiments, variable-wavelength density modulations could provide an ideal testbed to study anomalous transport in this system. Moreover, it would be particularly interesting to investigate the effect of integrability on transport in the one-dimensional mass-balanced Fermi-Hubbard model and explore the weak breaking of integrability by only slightly detuning the hopping amplitudes of the two species. Our work also motivates the experimental study of other quantum many-body systems with constraints originating from frustration and strong interactions, which can arise in Rydberg blockaded systems and in strongly tilted optical lattices [19, 24, 25].

ACKNOWLEDGMENTS

We acknowledge the valuable and helpful discussions with Dmitry A. Abanin, Johannes Feldmeier, Sarang Gopalakrishnan, Bharath Hebbe Madhusudhana, Markus Müller, Luis Riegger, Pablo Sala, Sebastian Scherg, Alessandro Silva, and we are grateful to Jesper Levinsen and Meera M. Parish for helpful insights on the orbital Feshbach resonance in an optical lattice. The authors also wish to thank Alexander Impertro for technical contributions to the experiment. This project has received funding from the Deutsche Forschungsgemeinschaft (DFG, German Research Foundation) under Germany's Excellence Strategy – EXC-2111 – 390814868,

DFG TRR80 and DFG grant No. KN1254/2-1, the European Research Council (ERC) under the European Union's Horizon 2020 research and innovation programme (grant agreement No. 817482 and No. 851161), and the Technical University of Munich – Institute for Advanced Study, funded by the German Excellence Initiative and the European Union FP7 under grant agreement 291763.

* n.darkwahoppong@lmu.de

- [1] J. M. Deutsch, Quantum statistical mechanics in a closed system, *Phys. Rev. A* **43**, 2046 (1991).
- [2] M. Srednicki, Chaos and quantum thermalization, *Phys. Rev. E* **50**, 888 (1994).
- [3] M. Rigol, V. Dunjko, and M. Olshanii, Thermalization and its mechanism for generic isolated quantum systems, *Nature (London)* **452**, 854 (2008).
- [4] L. D'Alessio, Y. Kafri, A. Polkovnikov, and M. Rigol, From quantum chaos and eigenstate thermalization to statistical mechanics and thermodynamics, *Adv. Phys.* **65**, 239 (2016).
- [5] I. Bloch, J. Dalibard, and W. Zwerger, Many-body physics with ultracold gases, *Rev. Mod. Phys.* **80**, 885 (2008).
- [6] R. Blatt and C. F. Roos, Quantum simulations with trapped ions, *Nat. Phys.* **8**, 277 (2012).
- [7] M. Kjaergaard, M. E. Schwartz, J. Braumüller, P. Krantz, J. I. J. Wang, S. Gustavsson, and W. D. Oliver, Superconducting Qubits: Current State of Play, *Annu. Rev. Condens. Matter Phys.* **11**, 369 (2020).
- [8] P. C. Hohenberg and B. I. Halperin, Theory of dynamic critical phenomena, *Rev. Mod. Phys.* **49**, 435 (1977).
- [9] S. Mukerjee, V. Oganesyan, and D. Huse, Statistical theory of transport by strongly interacting lattice fermions, *Phys. Rev. B* **73**, 035113 (2006).
- [10] J. Lux, J. Müller, A. Mitra, and A. Rosch, Hydrodynamic long-time tails after a quantum quench, *Phys. Rev. A* **89**, 053608 (2014).
- [11] A. Bohrdt, C. B. Mendl, M. Endres, and M. Knap, Scrambling and thermalization in a diffusive quantum many-body system, *New J. Phys.* **19**, 063001 (2017).
- [12] M. Schreiber, S. S. Hodgman, P. Bordia, H. P. Lüschen, M. H. Fischer, R. Vosk, E. Altman, U. Schneider, and I. Bloch, Observation of many-body localization of interacting fermions in a quasi-random optical lattice, *Science* **349**, 842 (2015).
- [13] S. Kondov, W. McGehee, W. Xu, and B. DeMarco, Disorder-Induced Localization in a Strongly Correlated Atomic Hubbard Gas, *Phys. Rev. Lett.* **114**, 083002 (2015).
- [14] J. Smith, A. Lee, P. Richerme, B. Neyenhuis, P. W. Hess, P. Hauke, M. Heyl, D. A. Huse, and C. Monroe, Many-body localization in a quantum simulator with programmable random disorder, *Nat. Phys.* **12**, 907 (2016).
- [15] P. Roushan, C. Neill, J. Tangpanitanon, V. M. Bastidas, A. Megrant, R. Barends, Y. Chen, Z. Chen, B. Chiaro, A. Dunsworth, A. Fowler, B. Foxen, M. Giustina, E. Jeffrey, J. Kelly, E. Lucero, J. Mutus, M. Neeley, C. Quintana, D. Sank, A. Vainsencher, J. Wenner, T. White,

- H. Neven, D. Angelakis, and J. Martinis, Spectroscopic signatures of localization with interacting photons in superconducting qubits, *Science* **358**, 1175 (2017).
- [16] R. Nandkishore and D. A. Huse, Many-Body Localization and Thermalization in Quantum Statistical Mechanics, *Annu. Rev. Condens. Matter Phys.* **6**, 15 (2015).
- [17] D. A. Abanin, E. Altman, I. Bloch, and M. Serbyn, Colloquium: Many-body localization, thermalization, and entanglement, *Rev. Mod. Phys.* **91**, 021001 (2019).
- [18] M. Serbyn, M. Knap, S. Gopalakrishnan, Z. Papić, N. Y. Yao, C. R. Laumann, D. A. Abanin, M. D. Lukin, and E. A. Demler, Interferometric Probes of Many-Body Localization, *Phys. Rev. Lett.* **113**, 147204 (2014).
- [19] H. Bernien, S. Schwartz, A. Keesling, H. Levine, A. Omran, H. Pichler, S. Choi, A. Zibrov, M. Endres, M. Greiner, V. Vuletic, and M. D. Lukin, Probing many-body dynamics on a 51-atom quantum simulator, *Nature (London)* **551**, 579 (2017).
- [20] C. J. Turner, A. A. Michailidis, D. A. Abanin, M. Serbyn, and Z. Papić, Weak ergodicity breaking from quantum many-body scars, *Nat. Phys.* **14**, 745 (2018).
- [21] R. M. Nandkishore and M. Hermele, Fractons, *Annu. Rev. Condens. Matter Phys.* **10**, 295 (2019).
- [22] A. Gromov, A. Lucas, and R. M. Nandkishore, Fracton hydrodynamics, *Phys. Rev. Research* **2**, 033124 (2020).
- [23] J. Feldmeier, P. Sala, G. de Tomasi, F. Pollmann, and M. Knap, Anomalous Diffusion in Dipole- and Higher-Moment Conserving Systems, [arXiv:2004.00635](https://arxiv.org/abs/2004.00635).
- [24] E. Guardado-Sanchez, A. Morningstar, B. M. Spar, P. T. Brown, D. A. Huse, and W. S. Bakr, Subdiffusion and Heat Transport in a Tilted Two-Dimensional Fermi-Hubbard System, *Phys. Rev. X* **10**, 011042 (2020).
- [25] S. Scherg, T. Kohlert, P. Sala, F. Pollmann, B. H. M., I. Bloch, and M. Aidelsburger, Observing non-ergodicity due to kinetic constraints in tilted Fermi-Hubbard chains, [arXiv:2010.12965](https://arxiv.org/abs/2010.12965).
- [26] Y. Kagan and L. A. Maksimov, Localization in a subsystem of interacting particles diffusing in a regular crystal, *JETP* **60**, 201 (1984).
- [27] W. De Roeck and F. Huveneers, Asymptotic Quantum Many-Body Localization from Thermal Disorder, *Comm. Math. Phys.* **332**, 1017 (2014).
- [28] M. Schiulaz, M. Müller, and M. Palassini, Ideal quantum glass transitions: Many-body localization without quenched disorder, *AIP Conf. Proc.* **1610**, 11 (2014).
- [29] M. Schiulaz, A. Silva, and M. Müller, Dynamics in many-body localized quantum systems without disorder, *Phys. Rev. B* **91**, 184202 (2015).
- [30] W. De Roeck and F. Huveneers, Scenario for delocalization in translation-invariant systems, *Phys. Rev. B* **90**, 165137 (2014).
- [31] Z. Papić, E. M. Stoudenmire, and D. A. Abanin, Many-body localization in disorder-free systems: The importance of finite-size constraints, *Ann. Phys.* **362**, 714 (2015).
- [32] N. Y. Yao, C. R. Laumann, J. I. Cirac, M. D. Lukin, and J. E. Moore, Quasi-Many-Body Localization in Translation-Invariant Systems, *Phys. Rev. Lett.* **117**, 240601 (2016).
- [33] J. Sirker, Exploration of the existence of a distinct quasi many-body localized phase: Numerical study of a translationally invariant system in the thermodynamic limit, *Phys. Rev. B* **99**, 075162 (2019).
- [34] Z. Lan, M. van Horssen, S. Powell, and J. P. Garrahan, Quantum Slow Relaxation and Metastability due to Dynamical Constraints, *Phys. Rev. Lett.* **121**, 040603 (2018).
- [35] J. Feldmeier, F. Pollmann, and M. Knap, Emergent Glassy Dynamics in a Quantum Dimer Model, *Phys. Rev. Lett.* **123**, 040601 (2019).
- [36] N. Pancotti, G. Giudice, J. I. Cirac, J. P. Garrahan, and M. C. Bañuls, Quantum East Model: Localization, Non-thermal Eigenstates, and Slow Dynamics, *Phys. Rev. X* **10**, 021051 (2020).
- [37] E. Guardado-Sanchez, B. M. Spar, P. Schauss, R. Belyansky, J. T. Young, P. Bienias, A. V. Gorshkov, T. Iadecola, and W. S. Bakr, Quench Dynamics of a Fermi Gas with Strong Long-Range Interactions, [arXiv:2010.05871](https://arxiv.org/abs/2010.05871).
- [38] A. D. Ludlow, M. M. Boyd, J. Ye, E. Peik, and P. O. Schmidt, Optical atomic clocks, *Rev. Mod. Phys.* **87**, 637 (2015).
- [39] L. Riegger, N. Darkwah Oppong, M. Höfer, D. R. Fernandes, I. Bloch, and S. Fölling, Localized Magnetic Moments with Tunable Spin Exchange in a Gas of Ultracold Fermions, *Phys. Rev. Lett.* **120**, 143601 (2018).
- [40] Z. W. Barber, J. E. Stalnaker, N. D. Lemke, N. Poli, C. W. Oates, T. M. Fortier, S. A. Diddams, L. Hollberg, C. W. Hoyt, A. V. Taichenachev, and V. I. Yudin, Optical Lattice Induced Light Shifts in an Yb Atomic Clock, *Phys. Rev. Lett.* **100**, 103002 (2008).
- [41] See Supplemental Material, which includes Refs. [57–70], for additional information about the experimental methods and a detailed discussion of the numerical simulations.
- [42] O. Bettermann, N. Darkwah Oppong, G. Pasqualetti, L. Riegger, I. Bloch, and S. Fölling, Clock-line photoassociation of strongly bound dimers in a magic-wavelength lattice, [arXiv:2003.10599](https://arxiv.org/abs/2003.10599).
- [43] L. Pezzè, L. Pitaevskii, A. Smerzi, S. Stringari, G. Modugno, E. de Mirandes, F. Ferlaino, H. Ott, G. Roati, and M. Inguscio, Insulating Behavior of a Trapped Ideal Fermi Gas, *Phys. Rev. Lett.* **93**, 120401 (2004).
- [44] H. Ott, E. de Mirandes, F. Ferlaino, G. Roati, G. Modugno, and M. Inguscio, Collisionally Induced Transport in Periodic Potentials, *Phys. Rev. Lett.* **92**, 160601 (2004).
- [45] G. Orso, L. P. Pitaevskii, and S. Stringari, Umklapp Collisions and Center-of-Mass Oscillations of a Trapped Fermi Gas, *Phys. Rev. Lett.* **93**, 020404 (2004).
- [46] M. Rigol and A. Muramatsu, Confinement control by optical lattices, *Phys. Rev. A* **70**, 043627 (2004).
- [47] M. Schulz, C. A. Hooley, and R. Moessner, Slow relaxation and sensitivity to disorder in trapped lattice fermions after a quench, *Phys. Rev. A* **94**, 063643 (2016).
- [48] G. H. Wannier, Dynamics of Band Electrons in Electric and Magnetic Fields, *Rev. Mod. Phys.* **34**, 645 (1962).
- [49] N. Strohmaier, Y. Takasu, K. Günter, R. Jördens, M. Köhl, H. Moritz, and T. Esslinger, Interaction-Controlled Transport of an Ultracold Fermi Gas, *Phys. Rev. Lett.* **99**, 220601 (2007).
- [50] M. Schulz, C. A. Hooley, R. Moessner, and F. Pollmann, Stark Many-Body Localization, *Phys. Rev. Lett.* **122**, 040606 (2019).
- [51] E. van Nieuwenburg, Y. Baum, and G. Refael, From Bloch oscillations to many-body localization in clean interacting systems, *Proc. Natl. Acad. Sci. U.S.A.* **116**, 9269 (2019).
- [52] T. Chanda, R. Yao, and J. Zakrzewski, Coexistence of

- localized and extended phases: Many-body localization in a harmonic trap, *Phys. Rev. Research* **2**, 032039(R) (2020).
- [53] U. Schneider, L. Hackermüller, J. P. Ronzheimer, S. Will, S. Braun, T. Best, I. Bloch, E. Demler, S. Mandt, D. Rasch, and A. Rosch, Fermionic transport and out-of-equilibrium dynamics in a homogeneous Hubbard model with ultracold atoms, *Nat. Phys.* **8**, 213 (2012).
- [54] B. Efron and C. Stein, The Jackknife Estimate of Variance, *Ann. Stat.* **9**, 586 (1981).
- [55] F. Jin, R. Steinigeweg, F. Heidrich-Meisner, K. Michielsen, and H. De Raedt, Finite-temperature charge transport in the one-dimensional Hubbard model, *Phys. Rev. B* **92**, 205103 (2015).
- [56] T. Heitmann, J. Richter, T. Dahm, and R. Steinigeweg, Density dynamics in the mass-imbalanced Hubbard chain, *Phys. Rev. B* **102**, 045137 (2020).
- [57] M. Kitagawa, K. Enomoto, K. Kasa, Y. Takahashi, R. Ciuryło, P. Naidon, and P. S. Julienne, Two-color photoassociation spectroscopy of ytterbium atoms and the precise determinations of s -wave scattering lengths, *Phys. Rev. A* **77**, 012719 (2008).
- [58] M. Köhl, Thermometry of fermionic atoms in an optical lattice, *Phys. Rev. A* **73**, 031601 (2006).
- [59] N. Darkwah Oppong, L. Riegger, O. Bettermann, M. Höfer, J. Levinsen, M. M. Parish, I. Bloch, and S. Fölling, Observation of Coherent Multiorbital Polarons in a Two-Dimensional Fermi Gas, *Phys. Rev. Lett.* **122**, 193604 (2019).
- [60] S. Friebel, C. D'Andrea, J. Walz, M. Weitz, and T. W. Hänsch, CO₂-laser optical lattice with cold rubidium atoms, *Phys. Rev. A* **57**, R20 (1998).
- [61] C. Chin, R. Grimm, P. Julienne, and E. Tiesinga, Feshbach resonances in ultracold gases, *Rev. Mod. Phys.* **82**, 1225 (2010).
- [62] E. K. Laird, Z.-Y. Shi, M. M. Parish, and J. Levinsen, Frustrated orbital Feshbach resonances in a Fermi gas, *Phys. Rev. A* **101**, 022707 (2020).
- [63] F. Verstraete, J. J. García-Ripoll, and J. I. Cirac, Matrix Product Density Operators: Simulation of Finite-Temperature and Dissipative Systems, *Phys. Rev. Lett.* **93**, 207204 (2004).
- [64] M. Zwolak and G. Vidal, Mixed-State Dynamics in One-Dimensional Quantum Lattice Systems: A Time-Dependent Superoperator Renormalization Algorithm, *Phys. Rev. Lett.* **93**, 207205 (2004).
- [65] J. Hauschild and F. Pollmann, Efficient numerical simulations with Tensor Networks: Tensor Network Python (TeNPy), *SciPost Phys. Lect. Notes* , 5 (2018).
- [66] S. Paeckel, T. Köhler, A. Swoboda, S. R. Manmana, U. Schollwöck, and C. Hubig, Time-Evolution Methods for Matrix-Product States, *Ann. Phys. (N. Y.)* **411**, 167998 (2019).
- [67] G. Vidal, Efficient Simulation of One-Dimensional Quantum Many-Body Systems, *Phys. Rev. Lett.* **93**, 040502 (2004).
- [68] R. Sensarma, D. Pekker, E. Altman, E. Demler, N. Strohmaier, D. Greif, R. Jördens, L. Tarruell, H. Moritz, and T. Esslinger, Lifetime of Double Occupancies in the Fermi-Hubbard Model, *Phys. Rev. B* **82**, 224302 (2010).
- [69] A. Auerbach, *Interacting Electrons and Quantum Magnetism* (Springer, New York, 1994).
- [70] M. Fava, B. Ware, S. Gopalakrishnan, R. Vasseur, and S. A. Parameswaran, Spin crossovers and superdiffusion in the one-dimensional Hubbard model, *Phys. Rev. B* **102**, 115121 (2020).

Supplemental Material

Probing transport and slow relaxation in the mass-imbalanced Fermi-Hubbard model

N. Darkwah Oppong,^{1,2,3,*} G. Pasqualetti,^{1,2,3} O. Bettermann,^{1,2,3}P. Zechmann,^{4,3} M. Knap,^{4,3} I. Bloch,^{1,2,3} and S. Fölling^{1,2,3}¹Ludwig-Maximilians-Universität, Schellingstraße 4, 80799 München, Germany²Max-Planck-Institut für Quantenoptik, Hans-Kopfermann-Straße 1, 85748 Garching, Germany³Munich Center for Quantum Science and Technology (MCQST), Schellingstraße 4, 80799 München, Germany⁴Department of Physics and Institute for Advanced Study, Technical University of Munich, 85748 Garching, Germany

(Dated: November 26, 2020)

CONTENTS

S.I. Experimental techniques	1
A. State preparation	1
B. Lattice loading	2
C. Absorption imaging	3
D. Hubbard parameters	3
E. Orbital Feshbach resonance	4
F. State-dependent lattice	5
G. Displacement of the trap center	5
H. Transport measurement	6
I. Density dynamics	7
S.II. Theoretical description	8
A. Non-interacting calculation	8
B. Many-body calculation	8
1. Initial state	9
2. Simulation of the transport measurement	10
C. Many-body Stark localization	10
D. Relaxation dynamics of the mass-balanced case	11
E. Time scales	11
References	12

S.I. EXPERIMENTAL TECHNIQUES

A. State preparation

The details on the preparation of degenerate gases of ^{171}Yb are described in Ref. [1] and we only briefly outline the procedure here. Our experiment starts by loading approximately 1.4×10^6 ^{174}Yb and 1.0×10^6 ^{171}Yb atoms from a magneto-optical trap (MOT) into a crossed optical dipole trap. We perform forced evaporation by lowering the optical dipole trap. Towards the end of the cooling sequence, we remove any remaining ^{174}Yb atoms with a resonant “push” pulse on the broad $^1\text{S}_0 \rightarrow ^1\text{P}_1$ transition. After evaporative cooling, typically $3\text{--}5 \times 10^3$ ^{171}Yb atoms in each of the two nuclear spin states $m_F \in \{-1/2, +1/2\}$ remain in the optical dipole trap at a temperature of $T \simeq 0.15T_F$, which is determined by fitting density profiles to in-situ absorption images. Here, T_F is the Fermi temperature. We note that the extremely small scattering length $-2.8(3.6)a_0$

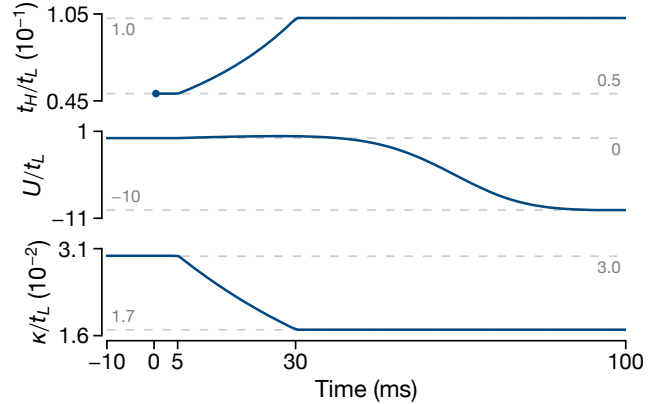


FIG. S1. Time dependence of the Hubbard parameters t_H , U , and κ during the state preparation for the target values $t_H/t_L \simeq 0.1$ and $U/t_L \simeq -10$. All parameters are estimated from the voltages controlling the lattice depth and magnetic field strength in the experiment. Time is given relative to the clock-laser excitation pulse which quenches the hopping ratio from $t_H/t_L = 1$ (not visible on the chosen scale) to $t_H/t_L \simeq 0.05$, indicated with a small circle.

of ^{171}Yb in the ground state [2] generally leads to a particularly long thermalization time scale. Here, a_0 is the Bohr radius.

The atoms are loaded into the optical lattices sequentially with s-shaped ramps, and we first ramp up the vertical state-independent lattice to $\approx 30 E_{\text{rec}}^m$ within 120 ms. Then, the state-independent lattice along the other axis is ramped up to the same depth within 300 ms. After subsequently loading the atoms into the $\approx 7E_{\text{rec}}$ deep state-dependent lattice (SDL) within 300 ms, we proceed with the state preparation (also see main text), which includes changing the SDL depth within 25 ms (linear ramp) and the magnetic field within 70 ms (s-shaped ramp) to set the desired Hubbard parameters. We show the time dependence of these values for an exemplary case in Fig. S1 and also refer to Table S1, which summarizes the experimental parameters for all figures in the main text.

We use a linearly polarized clock laser beam to excite atoms from the $|^1\text{S}_0, m_F = +1/2\rangle$ ground state (de-

TABLE S1. Experimental parameters for each figure presented in the main text. The lattice depth is given for the light species [$V_H = 3.06(4)V_L$ for the heavy species, see Section S.I.F]. We also show next-nearest neighbor and perpendicular hopping amplitudes to illustrate the accuracy of a one-dimensional tight-binding description.

	Fig. 2(a)	Fig. 3	Fig. 4(a)	Fig. 4(b)
Total number of light atoms N_{tot} (10^3)	4.2(3)	4.5(3)	3.3(4)	3.4(3)
Effective number of light atoms per tube $\mathcal{N}[\Delta\mathcal{N}]$	19[8]	19[9]	17[8]	17[8]
Lattice depth V_L (E_{rec})	0.69(3) - 11.8(5)	4.7(2)	3.1(1)	4.7(2)
Hopping amplitude t_L ($h \times \text{Hz}$)	33(4) - 488(2)	184(10)	283(8)	182(8)
Next-nearest neighbor hopping $t_L^{(2d)}/t_L$ (10^{-2})	0.75(10) - 21.8(2)	5.7(4)	9.9(4)	5.6(3)
Perpendicular hopping t_{\perp}/t_L (10^{-3})	2.1(3) - 31(8)	6(1)	3.7(6)	6(1)
Hopping ratio t_H/t_L	n/a	0.104(7)	0.203(8)	0.102(6)
Interaction strength U/t_L	n/a	-19(2) - 4.6(3)	-9.7(6) - 0.02(2)	-9.7(7) - 0.02(4)
Harmonic confinement κ/t_L (10^{-2})	0.63(3) - 9(1)	1.7(1)	1.10(7)	1.7(1)

noted $|g \uparrow\rangle$) to the $|^3P_0, m_F = +1/2\rangle$ clock state (denoted $|e \uparrow\rangle \equiv |H\rangle$). This laser beam co-propagates with one of the deep perpendicular lattices to drive the transition in the Lamb-Dicke regime. To overcome the inhomogeneous broadening present in the SDL and to quench the hopping amplitude for the heavy species, we use a high-intensity excitation pulse with Rabi frequency $\Omega \simeq 2\pi \times 3 \text{ kHz}$. We address singly and doubly occupied lattice sites with this single-frequency pulse by applying a large magnetic field $\simeq 1533 \text{ G}$ corresponding to the zero crossing of the orbital Feshbach resonance (see Section S.I.E), where the interaction shift of doubly occupied lattice sites vanishes. In general, the fidelity of the excitation pulse is fairly good, with $> 95\%$ of the atoms driven to $|H\rangle$. We note that the residual number of remaining $|g \uparrow\rangle$ atoms only interact with atoms in $|H\rangle$ (interaction strength $U_{H,g\uparrow} \gg t_L$). However, this is independent of the chosen heavy-light interaction strength and should only have a minor influence on our observations.

After quenching the hopping ratio t_H/t_L of the non-interacting mixture, we slowly ramp the interaction strength towards the desired value by varying the magnetic field accordingly [see Fig. S1]. In general, this process can significantly change the initial state, particularly the fraction of doublons as the Hamiltonian is gradually modified during the ramp of the interaction. However, coarse spectroscopic measurements and numerical simulations suggest that this fraction only weakly depends on the chosen U parameter [see Section S.II.B.1 for details].

B. Lattice loading

For the theoretical description of the experimental procedure (see Section S.II), the distribution of atoms across the different one-dimensional systems (tubes) is of central importance. Since our absorption imaging inherently averages across one axis, we cannot determine this quantity

directly. Instead, we estimate it from parameters in the dipole trap, together with the assumption of constant entropy during the process of lattice loading [3]. This assumption only approximately holds as we can detect an increase of the temperature (and entropy) by $\approx 30\%$ when loading the atoms from the lattice back into the dipole trap. We also simplify the lattice loading process by assuming the state-independent lattices are ramped up simultaneously (see Section S.I.A).

From the total number of light atoms N_{tot} , the trapping frequencies $(\omega_x, \omega_y, \omega_z) = 2\pi \times [38(1), 35(1), 402(1)] \text{ Hz}$ and temperature $T \simeq 0.15T_F$ in the optical dipole trap, we determine the total entropy $S(N_{\text{tot}}, T) \simeq N_{\text{tot}} \times 1.4k_B$ of the initial state. For the final state in the array of tubes formed by the perpendicular lattices, we fit the chemical potential μ_0 and temperature T' as parameters of the total entropy,

$$S'(\mu_0, T') = \sum_{i,j} S_{ij}(\mu_0 + \mu_{ij}, T'), \quad (\text{S.1})$$

under the constraint of constant entropy, $S = S'$, and conservation of atom number, $\sum_{i,j} N_{ij} = N_{\text{tot}}$. Here, S_{ij} is the entropy and N_{ij} the number of atoms in the (i, j) -th tube, described by a harmonically trapped one-dimensional Fermi gas. The chemical potential μ_{ij} accounts for the local offset of the harmonic potential from the optical dipole trap

$$\mu_{ij} = \frac{1}{2} m d_m^2 \left[\omega_y^2 (i + \varphi_i)^2 + \omega_z^2 (j + \varphi_j)^2 \right] \quad (\text{S.2})$$

with m the mass of a ^{171}Yb atom, $d_m = \lambda_m/2$ the spacing of the state-independent lattice, and φ_i, φ_j corresponding to the relative phase of the optical lattice and optical dipole trap. In Fig. S2(a), we plot the resulting distribution of $\{N_{ij}\}$ for typical parameters in our experiment. From this distribution, we also calculate the

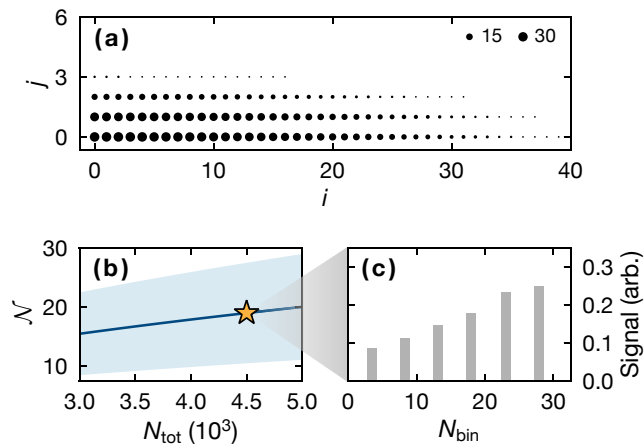


FIG. S2. Distribution of atoms across different one-dimensional systems (tubes). (a) Typical distribution of $N_{\text{tot}} = 4.5 \times 10^3$ (light) atoms across the tubes generated by the perpendicular state-independent lattices. Each black circle represents a tube with the size indicating the number of atoms (see legend). We only plot a single quadrant due to the symmetry of the distribution. (b) Effective number of light atoms per tube \mathcal{N} for variable total light atom numbers N_{tot} . The blue-shaded area corresponds to the region of $\mathcal{N} \pm \Delta\mathcal{N}$. (c) Approximate distribution of light atoms across different bins for $N_{\text{tot}} = 4.5 \times 10^3$ (yellow star) and their contribution to the measured signal. This distribution is obtained by averaging over multiple relative phases $-0.5 \leq \varphi_i, \varphi_j < 0.5$ [see Eq. (S.2)].

effective quantities shown in Table S1 and Fig. S2(b),

$$\mathcal{N} = \frac{1}{N_{\text{tot}}} \sum_{i,j} N_{ij}^2, \text{ and} \quad (\text{S.3})$$

$$\Delta\mathcal{N} = \left[\frac{1}{N_{\text{tot}}} \sum_{i,j} N_{ij} (\mathcal{N} - N_{ij})^2 \right]^{1/2}. \quad (\text{S.4})$$

For our theoretical calculations (see Section S.II A), we distribute $\{N_{ij}\}$ over six bins such that the effective width of each bin is approximately constant and average over ten relative phases for each φ_i and φ_j [see Fig. S2(c)]. We only consider the ≈ 300 significantly filled tubes ($N_{ij} \geq 1$) in this procedure, which account for more than 98% of the signal.

Finally, we calculate all relevant parameters in the state-dependent lattice using the atom numbers $\{N_{ij}\}$ and entropies $\{S_{ij}\}$, which we increase by $30\%/2 = 15\%$ to account for half of the temperature increase observed when loading back into the optical dipole trap. From this estimate and the exact diagonalization of the single-particle Hamiltonian in Eq. (S.14), we find an effective filling $n \simeq 0.5$, fraction of doublons $\mathcal{D} \simeq 0.3$, and temperature $T \simeq 2t_L/k_B$ for a typical total number of light atoms $N_{\text{tot}} = 4.5 \times 10^{-3}$ and lattice depth $V_L = 4.7E_{\text{rec}}$. In addition, we estimate the effective sys-

tem size $l \approx 30$ lattice sites of a typical tube from the root-mean-square width of the density distribution along the one-dimensional system, which is also obtained with exact diagonalization techniques (see Section S.II A).

C. Absorption imaging

We perform in-situ absorption imaging of the atomic cloud on the broad $^1S_0^{F=1/2} \rightarrow ^1P_1^{F=3/2}$ transition, which allows us to directly determine the column density of the light atoms. In the experiment, we freeze the atomic density by rapidly increasing the lattice depth to $\approx 15E_{\text{rec}}$ within 2.5 ms. Then, we lower the magnetic field within 30 ms to 2 G and image the light atoms with a $5 \mu\text{s}$ long high-intensity pulse. To calibrate the atomic cross-section and the absolute atom number, we use a technique analog to the one used for ^{173}Yb in Ref. [4].

Finally, we briefly comment on the indirect imaging of the heavy atoms, which are detected after the first imaging pulse has removed all light atoms in the 1S_0 state. We employ a 3 ms long laser pulse resonant with the $^3P_0^{F=1/2} \rightarrow ^3D_1^{F=3/2}$ transition to repump all clock state (heavy) atoms back to the ground state. Subsequently, these atoms are detected with absorption imaging on the same transition as the light atoms. However, this detection technique does not reliably determine the in-situ density of the heavy atoms for several technical reasons. First, the repumping introduces motional blurring and additional atom loss up to 30% [1], which depends significantly on the local density. Second, on-site heavy-light atom pairs can either be projected onto the repulsive branch or are continuously transferred into the deeply bound molecular state [1] during the relatively quick ramp of the magnetic field before the imaging. The exact process strongly depends on the technical details of the ramp, and our data suggests that heavy atoms transferred to the molecular state are dark for our detection method, thereby introducing additional loss on the order of $\sim 10\%$. Although the generally $\approx 40\%$ lower number of detected heavy atoms [see Figs. S7(c) and S7(d)] is approximately consistent with our estimates, the measured column densities still contain systematic errors, and we therefore do not use them for any quantitative analysis.

D. Hubbard parameters

We determine the hopping amplitudes t_L and t_H from two separate tight-binding band structures for light and heavy atoms [5]. The on-site interaction U is determined from the overlap of the Wannier functions $w_\alpha(x)$ and the

magnetic field-dependent s -wave scattering length a (see Section S.I.E),

$$U = \frac{4\pi\hbar^2 a}{m} \int d\mathbf{r} |w_L(x)|^2 |w_H(x)|^2 |w_\perp(y, z)|^4. \quad (\text{S.5})$$

Here, $\mathbf{r} = (x, y, z)$, m is the mass of a ^{171}Yb atom, and $w_\perp(y, z) = w_y(y)w_z(z)$ is the combined Wannier function along the perpendicular axes y and z . The main experimental input parameters for the band structure calculations are the lattice wavelength and depth. The former is fixed with high precision by locking the lasers to a wavelength meter using a digital servo. In contrast, the latter is calibrated for each measurement using deep lattices to minimize systematic uncertainties. For this calibration, we employ lattice modulation spectroscopy [6] for one of the state-independent lattice axes and resolved sideband spectroscopy on the clock transition for the remaining two lattice axes (state-independent and state-dependent, also see Section S.I.F). From these measurements, we also estimate the uncertainties of the Hubbard parameters. Finally, the value of the confinement parameter $\kappa = m\omega^2 d^2$ is obtained by measuring the trapping frequency ω after suddenly displacing the trap center and fitting the frequency of the resulting center-of-mass oscillations. We perform this measurement with the state-dependent lattice turned off as it does not significantly contribute to the confinement.

E. Orbital Feshbach resonance

Details on the orbital Feshbach resonance (OFR) in ^{171}Yb can be found in Ref. [1]. Here, we only briefly discuss how we employ clock-line spectroscopy on the single-particle and two-particle resonance to measure the magnetic field-dependent s -wave scattering length between $|e \uparrow\rangle \equiv |H\rangle$ and $|g \downarrow\rangle \equiv |L\rangle$ atoms. This measurement is performed in a nearly isotropic three-dimensional state-independent optical lattice with depth $\approx 30.7(8)E_{\text{rec}}$ to avoid the inhomogeneous broadening present in the state-dependent lattice (SDL). From the transition energies at various magnetic fields B , we extract the corresponding scattering length $a(B)$ with an expression similar to Eq. (S.5). In Fig. S3, we show the experimental data together with a fit to the following general form [7],

$$a(B) = a_{\text{bg}} \left[1 - \frac{\Delta}{(B - B_0)} \right]. \quad (\text{S.6})$$

Here, the fit parameters are $a_{\text{bg}} = 333(14)a_0$, $\Delta = 255(6)$ G, and $B_0 = 1285(5)$ G with a_0 the Bohr radius.

We find a significant dependence of the zero crossing $B_{a=0} = B_0 + \Delta$ (calculated from the fitted parameters) on the chosen lattice depth (see inset of Fig. S3). The effective shift of $B_{a=0}$ most likely originates from the energy dependence of the open-channel scattering ampli-

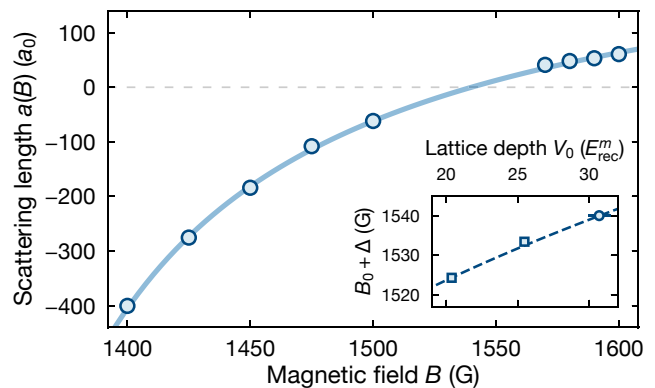


FIG. S3. Scattering length extracted from clock-line spectroscopy of the single- and two-particle resonance in a nearly isotropic three-dimensional state-independent optical lattice with depth $V_0 = 30.7(8)E_{\text{rec}}^m$. The circles correspond to individual data points and the solid line is a fit to Eq. (S.6). We do not plot data points close to $a(B) = 0$ since the resonances overlap in this region making the fit of the experimental data prone to systematic errors. In the inset, we show the zero crossing ($B_0 + \Delta$) in an isotropic state-independent optical lattice with variable depth. Here, the circle corresponds to the data set in the main panel whereas the squares represent separate measurements. The dashed line shows the expected scaling from Eq. (S.7) relative to the data point $V_0 = 30.7E_{\text{rec}}^m$.

tude [8]. For the lattice depth V_0 , the zero-point energy of the ground band is approximately given by

$$\epsilon_0 \simeq \frac{3}{2} \left(\frac{V_0}{E_{\text{rec}}^m} - \frac{1}{4} \right)^{1/2} E_{\text{rec}}^m \quad (\text{S.7})$$

and the resulting shift of the zero crossing can be obtained from $\delta B_{a=0} = \epsilon_0/|\delta u|$ with $\delta u = -h \times 399.0(1)$ Hz the differential Zeeman shift of the open and closed channel [1, 8]. In this simple approximation, we neglect any energy dependence of the scattering length itself but still find good agreement between experiment and theory. The situation for the SDL is slightly different, and we have to consider the mean zero-point energy of a light and a heavy atom in combination with different optical lattices. We utilize the symmetry (with respect to $U = 0$) of the signal in Fig. 3 and benchmark our approach with additional measurements for different depths of the SDL [see Fig. S5(c)]. Since we do not know the precise location of the zero crossing without the trap, we extract it from a fit to this data.

Finally, we briefly comment on the lifetime of the heavy-light mixture close to the OFR, which we can monitor up to a maximum duration of 400 ms in our experiment. In general, losses over this time scale are relatively small for the regime 1450-1600 G but increase quickly for magnetic fields $\lesssim 1450$ G. Importantly, these losses should be negligible for most magnetic fields employed for the measurements in the main text [also see Figs. S7(c) and S7(d)].

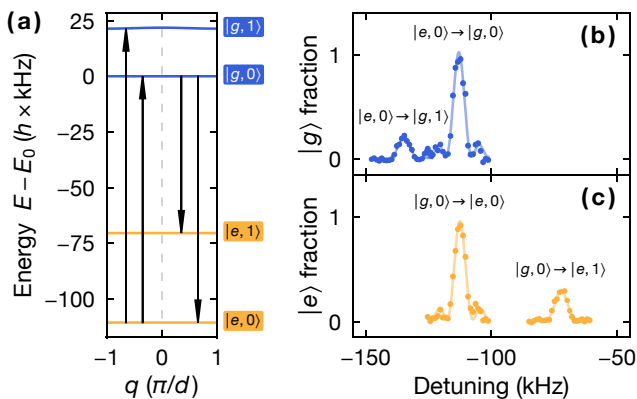


FIG. S4. Measurement of the polarizability ratio p in the state-dependent lattice (SDL). (a) Band structure of a $22.6(6)E_{\text{rec}}$ deep SDL with the two lowest-lying energy bands of $|g\rangle$ atoms (blue) and $|e\rangle$ atoms (yellow). The four transitions required to determine the $|g\rangle$ and $|e\rangle$ band gap are shown as black arrows at exemplary quasi-momenta q . All energies are shown relative to E_0 , which is the mean energy of the $|g\rangle$ ground band. (b),(c) Clock-line spectra of the carrier and sideband transitions starting from (b) $|e, 0\rangle$ and (c) $|g, 0\rangle$ for variable detuning of the clock laser. Here, the circles correspond to data points and the solid lines to individual fits of the line shapes.

F. State-dependent lattice

Our state-dependent optical lattice (SDL) is generated by retro-reflecting a monochromatic laser beam with wavelength $\lambda = 671.509(1)$ nm, almost identical to the realization in Ref. [9]. At this particular wavelength, the polarizability α of $|g\rangle$ (light) and $|e\rangle$ (heavy) atoms differs significantly, giving rise to different lattice depths and hopping amplitudes. We determine the corresponding polarizability ratio $p = \alpha_e/\alpha_g = V_H/V_L$ with interleaved sideband spectroscopy on the clock transition. Here, V_H and V_L are the lattice depths experienced by heavy ($|e\rangle$) and light ($|g\rangle$) atoms, respectively.

For this measurement, we use a separate clock laser beam co-aligned with the SDL axis to change the orbital state from $|g\rangle$ to $|e\rangle$ (or vice versa) and simultaneously the band index from m to m' . We perform two sets of measurements, one with the atoms initially prepared in $|e, m = 0\rangle$ and the other with the atoms in $|g, m = 0\rangle$. By driving the carrier ($m = 0 \rightarrow m' = 0$) as well as the first sideband transition ($m = 0 \rightarrow m' = 1$), we find two transition frequencies by fitting the line shapes as shown in Figs. S4(b) and S4(c). Subtracting the two frequencies yields the band gap individually for $|g\rangle$ and $|e\rangle$ atoms, which allows us to determine the corresponding lattice depths V_L and V_H from a band-structure calculation. With these results, we find a polarizability ratio $p = 3.06(4)$ from multiple measurements.

The much larger polarizability α_e of the clock state

3P_0 ($|e\rangle$) arises since the SDL is operated only ≈ 20 nm detuned from the ${}^3P_0 \rightarrow {}^3S_1$ transition wavelength. Consequently, the scattering of lattice photons becomes significant and heavy atoms off-resonantly excited to the 3S_1 state quickly decay back to either of the lower-lying ${}^3P_{J=0,1,2}$ states with a ratio of 15 : 40 : 45 according to the Clebsch-Gordan coefficients. Thus, the scattering of only two photons is sufficient to almost completely deplete the $|e\rangle$ state, and the dominant dissipation in the system is the loss of heavy atoms. More precisely, heavy atoms are converted with almost equal probability to either 3P_1 atoms with a subsequent quick decay back to $|g \uparrow\rangle$ or 3P_2 atoms, which are long-lived and dark.

We characterize the loss dynamics by monitoring the remaining number of heavy atoms after preparing a pure sample in $|e \uparrow\rangle = |H\rangle$. For the relevant lattice depths ($3-7E_{\text{rec}}$), we find $1/e$ lifetimes $\sim 10^3\hbar/t_L$ obtained by fitting the experimental data. While these loss rates are negligible for probing the transport directly after the displacement of the trap minimum in Fig. 3, the total loss becomes appreciable with $\approx 20\%$ for the longest observation times $\simeq 400\hbar/t_L$ of the density dynamics in Fig. 4.

G. Displacement of the trap center

We use an off-centered state-independent dipole trap beam operated at the magic wavelength to displace the minimum of the trap. The spatially-dependent potential resulting from this approximately Gaussian laser beam is given as

$$U_{\Delta}(x) = \frac{1}{2}m\omega_{\Delta}^2(x - x_{\Delta})^2 \left\{ 1 + \mathcal{O}\left[\frac{(x - x_{\Delta})^2}{w_0^2}\right] \right\}. \quad (\text{S.8})$$

Here, m is the mass of a ${}^{171}\text{Yb}$ atom, $\omega_{\Delta} \in 2\pi \times [0, 23]$ Hz is the trapping frequency proportional to the chosen intensity of the laser beam, $x_{\Delta} \approx 50 \mu\text{m}$ is the displacement of the beam with respect to the initial trap minimum i_0 (see main text), and $w_0 \approx 1.2x_{\Delta}$ is the estimated waist of the Gaussian laser beam. Neglecting the higher-order corrections to $U_{\Delta}(x)$, the shifted location of the trap center x_0 is given as

$$\Delta x = x_{\Delta} \frac{\omega_{\Delta}^2}{\omega^2 + \omega_{\Delta}^2} \quad (\text{S.9})$$

with $\omega = 40(1)$ Hz (see main text). For our measurements discussed in the main text, the intensity $I_{\Delta} \propto \omega_{\Delta}^2$ of the off-centered dipole trap is linearly increased, such that the trap minimum is displaced accordingly. We note that the terms in Eq. (S.8) also modify the effective trapping frequency ω , which we estimate to be on the order of $\sim 10\%$ and neglect in our theoretical description.

We calibrate the final value of Δx independently by ramping up the dipole trap before loading the state-dependent lattice. This allows us to extract the trap

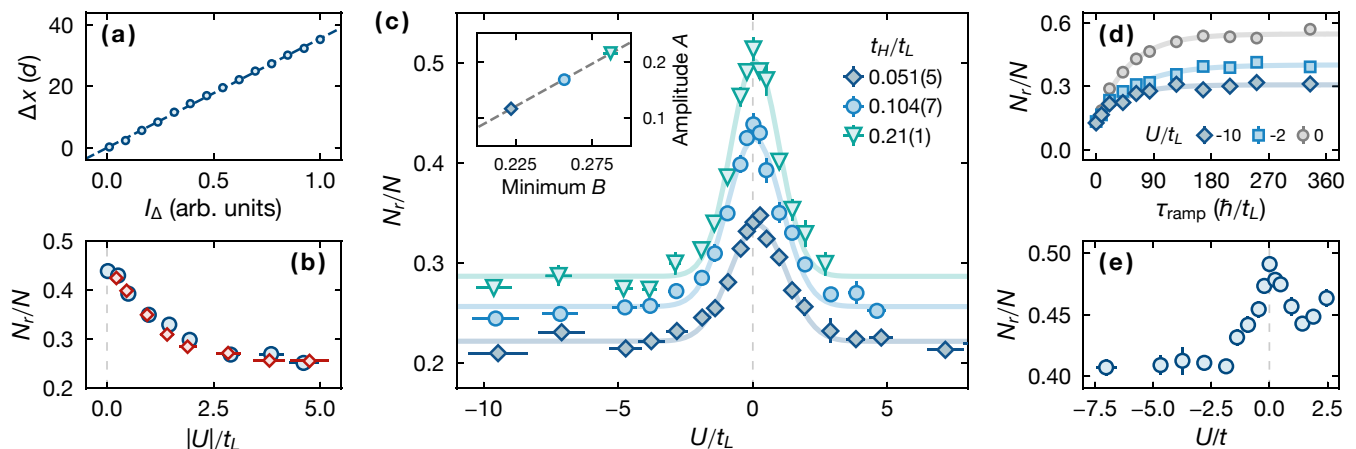


FIG. S5. Details on the displacement of the trap center and the transport measurement. (a) Transport distance Δx extracted from a Gaussian fit of the atomic column density for variable intensity I_Δ in the off-centered dipole trap. The dashed line corresponds to a linear fit. (b) Transported fraction N_r/N from Fig. 3 shown for $|U|/t_L$ to illustrate the symmetry between attractive ($U < 0$, red diamonds) and repulsive ($U > 0$, blue circles) interactions. (c) Transported fraction N_r/N for variable hopping ratio t_H/t_L and interaction strength U/t_L . Note that the $t_H/t_L = 0.104(7)$ data set (light blue circles) corresponds to the data shown in Fig. 3. The solid lines are fits to $A \exp[-(U/t_L)^2/(2\sigma^2)] + B$ for extracting the amplitude A and minimum B shown in the inset together with a linear fit (dashed gray line). (d) Transported fraction N_r/N for $t_H/t_L = 0.102(6)$, $\Delta x \simeq 43(3)d$, and variable ramp duration τ_{ramp} . The solid lines are a guide to the eye. (e) Transported fraction N_r/N for the special case $t \equiv t_H = t_L$ and variable interaction strength U/t with the transport distance $\Delta x \simeq 44(3)d_m$ and ramp duration $94(3)\hbar/t$.

center and effective displacement from a Gaussian fit of the atomic column density. In Fig. S5(a), we show the result of such fits for variable intensity of the optical dipole trap. We estimate the statistical uncertainty of Δx conservatively with $\approx 3d$ from the observed 2σ -fluctuations of the trap center over typical measurement durations.

H. Transport measurement

In this section, we discuss details and show additional experimental data for the transport measurements. As discussed in the main text, we observe a mostly symmetric signal (see Fig. 3), which only depends on the absolute value of the interaction strength $|U|/t_L$, shown explicitly in Fig. S5(b). Formally, the dynamical symmetry of our model in the limit $\kappa = 0$ [10] is broken by the finite confinement. Due to the relatively small energy scale of κ , we nevertheless still expect the dynamics to be comparable for attractive and repulsive interactions, which is confirmed by our numerical simulations shown in Fig. 3 [also see Section S.II B 2].

In Fig. S5(c), we show additional measurements for the hopping ratios $t_H/t_L \simeq 0.05$ and 0.2 obtained by adjusting the depth of the state-dependent lattice (SDL) accordingly. We note that this also changes the relative confinement to $\kappa/t_L = 2.9(3) \times 10^{-2}$ and $1.1(1) \times 10^{-2}$ compared to the case of $t_H/t_L \simeq 0.1$ discussed in the main text. In general, we observe a similar functional dependence on the interaction parameter, but the overall

amplitude and value for $U/t_L \simeq 0$ is reduced for smaller hopping ratios, which we attribute to a larger fraction of atoms occupying Stark-localized states. The inset in Fig. S5(c) illustrates the approximate linear behavior, which we find between the amplitude and minimum of a Gaussian fit.

To determine the optimal speed for the translation of the trap minimum in our measurement, we also characterize the transported fraction N_r/N for constant ramp distance Δx and variable ramp duration τ_{ramp} . For the probed interaction parameters $U/t_L \simeq 0, -2, -10$, we find a monotonous increase of the observable, which approximately follows an exponential saturation curve, as shown in Fig. S5(d). For the measurements in the main text, we chose the ramp speed $\approx 0.5dt_L/\hbar$, which corresponds to approximately twice the $1/e$ time in the non-interacting case. We note that the transported fraction N_r/N remains significantly reduced for all finite interactions and independent of the exact ramp duration.

To complement the data in Fig. 3, we perform an additional measurement for a mass-balanced configuration with $t \equiv t_L = t_H$. This is achieved by replacing the SDL with a state-independent lattice operated at the magic wavelength with the same lattice depth for the $|L\rangle$ as well as $|H\rangle$ state. We emphasize that this measurement only serves as a qualitative comparison since the beam parameters of the two lattices differ strongly, which introduces systematic differences. In general, we observe a much smaller suppression of the transported fraction and a large asymmetry between attractive ($U < 0$) and repul-

sive ($U > 0$) interactions [see Fig. S5(e)]. In contrast to the situation in the SDL, the fraction of doublons here strongly depends on the interaction parameter due to the nearly adiabatic state preparation. Thus, the inhibited transport originates most likely from the slow dynamics $\propto t^2/U$ of doublons in the system, as similarly observed in Ref. [11]. We verify the increased (reduced) doublon fraction for attractive (repulsive) interactions with clock-line spectroscopy and find a modulation of up to $\approx 50\%$ —in reasonable agreement with the observed asymmetric lineshape.

I. Density dynamics

We characterize the non-equilibrium dynamics after the displacement of the trap minimum for variable hold times by recording the density deviation,

$$\delta n(\tau) = \left\{ \int dx n(x, \tau) [n(x, \tau) - n(x, 0)]^2 \right\}^{(1/2)}, \quad (\text{S.10})$$

as discussed in the main text. The effective weight $n(x, \tau)$ helps to significantly reduce the contribution of noise in the integral. The one-dimensional density $n(x, \tau)$ is calculated from the two-dimensional atomic column density $\text{CD}(x, y; \tau)$ by normalization and integration along y ,

$$n(x, \tau) = \frac{1}{\int dx dy \text{CD}(x, y; \tau)} \int dy \text{CD}(x, y; \tau). \quad (\text{S.11})$$

The relaxation of $n(x, \tau)$ shown explicitly in the two right panels of Fig. 4 for $t_H/t_L \simeq 0.1$ and $U/t_L \simeq -10, 0$ can also be observed for other interaction parameters and hopping ratios, which are shown in Fig. S6. Importantly, the signatures of $\delta n(\tau)$ discussed in the main text can also be similarly found in the fraction of transported atoms N_r/N . However, this observable is particularly sensitive to the exact calibration of the trap minimum i_0 (see Section S.I.G) as the atomic cloud does not fully separate for the relatively short transport distance $\Delta x \simeq 20d$ in this measurement. Additionally, we note that the center of mass determined for each $n(x, \tau)$ shows interaction-dependent dynamics with similar features as $\delta n(x, \tau)$.

Since the observable $\delta n(\tau)$ rectifies any differences between $n(x, 0)$ and $n(x, \tau)$, it is susceptible to technical noise. To estimate the contribution of noise to our observable, we consider the density variance δn^2 and assume noise n_ϵ with vanishing mean $\langle n_\epsilon \rangle = 0$, finite variance $\langle n_\epsilon^2 \rangle > 0$, and vanishing third moment $\langle n_\epsilon^3 \rangle = 0$. Here, $\langle X \rangle$ denotes the expectation value of the quantity X . From these assumptions and Eq. (S.10), we find that the contribution of n_ϵ to δn^2 is proportional to $\langle n_\epsilon^2 \rangle$. We therefore expect for uncorrelated n_ϵ ,

$$\delta n_M^2(\tau) = \frac{\langle n_\epsilon^2 \rangle}{M} + \delta n^2(\tau) = \frac{\gamma}{M} + \delta n^2(\tau). \quad (\text{S.12})$$

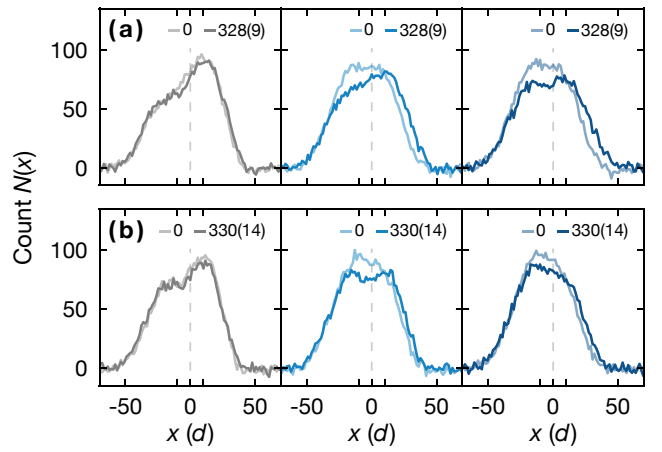


FIG. S6. One-dimensional densities for the hopping ratios (a) $t_H/t_L = 0.203(8)$ and (b) $0.102(6)$ and two distinct hold times $\tau \simeq 0, 330\hbar/t_L$ as indicated in the top right legend of each panel (units of \hbar/t_L). From left to right, $U/t_L = 0.02(4)$ (gray), $-1.9(2)$ (light blue), and $-9.7(7)$ (dark blue).

Here, γ is a constant, M is the number of individual measurements averaged for the calculation of $n(x, \tau)^2$ and δn_M^2 is the experimental measurement as opposed to the measurement-independent observable δn^2 . The value δn_M^2 for $M \leq 4$ can be estimated from subsampling since we take four individual measurements for each parameter. This allows us to extract the otherwise unknown value of δn^2 and γ from a fit. To avoid systematic errors, we use non-interacting data points in the stationary regime and find the noise contribution $\delta n_{M=4}(\tau) - \delta n(\tau) \simeq 0.4 \times 10^{-3}$, which is used to indicate the band of the theory data in Fig. 4. We emphasize that this approach only serves as an estimate since it neglects potential correlations of n_ϵ .

In Figs. S7(c) and S7(d), we show the number of heavy and light atoms during the measurement of the density dynamics. The initial atom numbers and loss rates of the heavy species are generally quite comparable for the different interaction parameters except for the $U/t_L \simeq -10$, $t_H/t_L \simeq 0.2$ dataset which was taken at a particular small magnetic field of ≈ 1410 G where the losses are increased due to the vicinity of the orbital Feshbach resonance (see Section S.I.E).

For the comparison of the relaxation time scales with the theoretical predictions for the mass-balanced Fermi-Hubbard model discussed in the main text, we fit the experimental data shown in Fig. 4(a) with a saturation curve, given by

$$\delta n(\tau) = A \left(1 - e^{-\tau/\tau_0} \right) + B. \quad (\text{S.13})$$

Here, A, B are dimensionless fit parameters, and τ_0 is the fitted time scale, which is discussed and compared to τ^* in the main text. In Fig. S8, we show the data

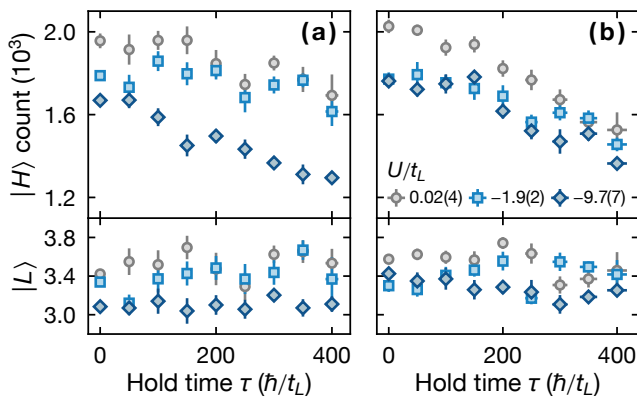


FIG. S7. Atom loss during the measurement of the density deviation $\delta n(\tau, x)$. (a),(b) Number of heavy ($|H\rangle$), top panels and light ($|L\rangle$), bottom panels) atoms during the measurement of the density deviation for (a) $t_H/t_L \simeq 0.2$ and (b) $t_H/t_L \simeq 0.1$ presented in Fig. 4. Data points spaced less than $50\hbar/t_L$ are binned to reduce visual clutter, and the interaction parameters are shown in the legend.

and fit, which agree reasonably well. We note that the data is only fitted for hold times $\tau > 1\hbar/t_L$ in analogy to the analysis of the theoretical data for the mass-balanced Fermi-Hubbard model (see Section S.IID).

S.II. THEORETICAL DESCRIPTION

A. Non-interacting calculation

For the theoretical calculations in the non-interacting limit (see Figs. 2 and 4), we employ the following single-particle Hamiltonian

$$\hat{\mathcal{H}}^{(1)} = -t_L \sum_i \hat{c}_{iL}^\dagger \left[\hat{c}_{(i+1)L} + \text{h.c.} \right] + \frac{\kappa}{2} \sum_i (i - i_0)^2 \hat{n}_{iL}, \quad (\text{S.14})$$

which we numerically diagonalize for a finite but large system size $l = 250$ ($i \in [-l/2, l/2]$) to find the eigenenergies ϵ_k and eigenstates

$$|\psi_k\rangle = \sum_{i=-l/2}^{l/2} \alpha_i^{(k)} \hat{c}_{iL}^\dagger |0\rangle \quad (\text{S.15})$$

with time evolution $|\psi_k(\tau)\rangle = e^{-i\epsilon_k\tau/\hbar} |\psi_k\rangle$. To account for the finite temperature T of the system (see Section S.IB), we calculate the occupation of the different eigenstates from the Fermi-Dirac distribution

$$f(\epsilon_k, T) = \frac{1}{e^{(\epsilon_k - \mu_0)/(k_B T)} + 1}. \quad (\text{S.16})$$

Here, T is the temperature, and the chemical potential $\mu_0 = \mu(N_L, T)$ is fixed by the constraint $\sum_k f(\epsilon_k, T) =$

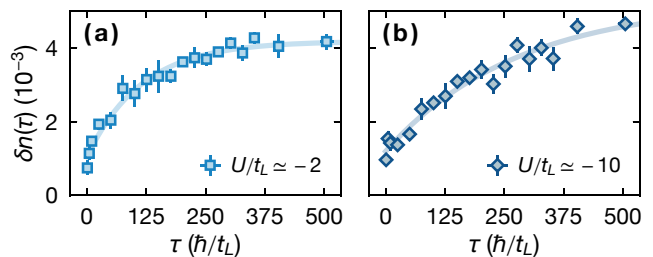


FIG. S8. Fits of the density deviation $\delta n(\tau \geq 1\hbar/t_L)$ for $t_H/t_L = 0.203(8)$ and (a) $U/t_L \simeq -2$ as well as (b) -10 . The solid lines correspond to the fit described by Eq. (S.13) with the extracted time scale (a) $\tau_0 = 116(15)\hbar/t_L$ and (b) $278(68)\hbar/t_L$. We note that the data point at $\tau \simeq 500\hbar/t_L$ is not shown in Fig. 4(a).

N_L with N_L the total number of light atoms in one tube. Finally, we calculate the time-dependent density profile

$$n(i, \tau) = \sum_k f(\epsilon_k, T) \left| \langle \psi_k(\tau) | \hat{c}_{iL}^\dagger | 0 \rangle \right|^2 \quad (\text{S.17})$$

from which we determine the experimentally relevant quantities.

The ramp of the trap minimum in the experiment is simulated by integrating the time-dependent Schrödinger equation corresponding to the Hamiltonian (S.14) for all eigenstates. For the long evolution times in Fig. 4, we average the calculation over ten equally spaced non-integer offsets $\in [-0.5, 0.5)$ of the trap minimum relative to i_0 . This is motivated by the fact that the relative phase of the lattice with respect to the minimum of the harmonic confinement is not fixed between individual shots of the experiment and also varies across the different tubes. To approximately model the contributions of tubes with different atom numbers in the experiment, we use a binned distribution with different weights (see Section S.IB) calculated for the specific total number of light atoms N_{tot} (see Table S1) and estimate our observable from a weighted average of these bins. The theory curve in Fig. 2 systematically overestimates N_r/N , which can be corrected with a $\approx 25\%$ increase of the estimated temperature or atom number. We observe a similar deviation for the experimental and theoretical data in Fig. 4. Overall, we attribute the disagreement to the approximative nature of our modeling of the lattice loading process.

B. Many-body calculation

To study the interacting Hamiltonian defined in Eq. (1) we employ tensor network methods as we aim to closely predict the dynamics observed in the experiment. To account for the finite temperature of the system, we apply a density matrix-based approach, where the density matrix ρ of the closed system is approximated as a

matrix-product operator (MPO). By means of purification, this MPO can be expressed as pure matrix-product state (MPS) $|\rho\rangle$ in an enlarged Hilbert space, such that we obtain the density matrix by tracing out the ancilla degrees of freedom $\hat{\rho} = \text{Tr}_a |\rho\rangle\langle\rho|$. In this representation, we can make use of established tensor network algorithms developed in the MPS framework [12, 13]. In particular, we implement our code based on the TenPy package [14]. To calculate the thermal equilibrium state $\hat{\rho} \propto e^{-\beta\hat{H}}$ we start with the maximally mixed, infinite temperature state $\hat{\rho}_0 \propto \mathbb{1}$, which can be represented exactly as a trivial MPO. For our nearest-neighbor Hamiltonian we employ the time evolving block decimation (TEBD) algorithm [15, 16] to obtain the equilibrium state at $T = 1/(k_B\beta)$,

$$\hat{\rho} \propto \text{Tr}_a \left[e^{-\beta/2\hat{H}} |\rho_0\rangle\langle\rho_0| e^{-\beta/2,\hat{H}} \right], \quad (\text{S.18})$$

by evolving $|\hat{\rho}_0\rangle$ up to $\beta/2$ in imaginary time. The dynamics of our system are governed by the von Neumann equation $\partial_\tau \hat{\rho} = -i[\hat{H}, \hat{\rho}]$, which we can write in terms of the purified MPS,

$$\partial_\tau |\rho\rangle = -i\mathcal{L} |\rho\rangle, \quad (\text{S.19})$$

with the Liouville superoperator $\mathcal{L} = \hat{H} \otimes \mathbb{1} - \mathbb{1} \otimes \hat{H}$. The solution $|\rho(\tau)\rangle = e^{-i\mathcal{L}\tau} |\rho\rangle$ can be efficiently calculated by propagating the initial state in real time with the TEBD algorithm. The accuracy of our simulations depends critically on the operator-space entanglement, defined as the half-chain von Neumann entanglement entropy corresponding to the normalized MPS $|\rho\rangle$. Throughout our simulations, we dynamically truncate the singular values at each bond, by keeping the discarded weight smaller than a threshold $\varepsilon_{\text{trunc}}$, but keeping at most χ_{max} Schmidt values. Note that in order to keep truncation errors negligible at fixed χ_{max} , our simulations are generally restricted to small atom numbers $N_L = N_H \leq 10$.

1. Initial state

In general, we expect that the details of our initial state preparation in the experiment (see Section S.I.A) have an important influence on the dynamics. Therefore, we study the preparation protocol numerically by approximating the time dependence of the Hubbard parameters [see Fig. S1] with a sequence of linear ramps and intermediate hold times. We integrate the von Neumann equation for the time-dependent Hamiltonian by applying the TEBD algorithm with a first-order Trotter decomposition, while updating the time evolution operator within each simulation step. This procedure resembles the simplest possible unitary integration scheme within our MPS approximation. We start with a non-interacting thermal state at $T_{\text{init}} = 4t_L/k_B$ to approximately model

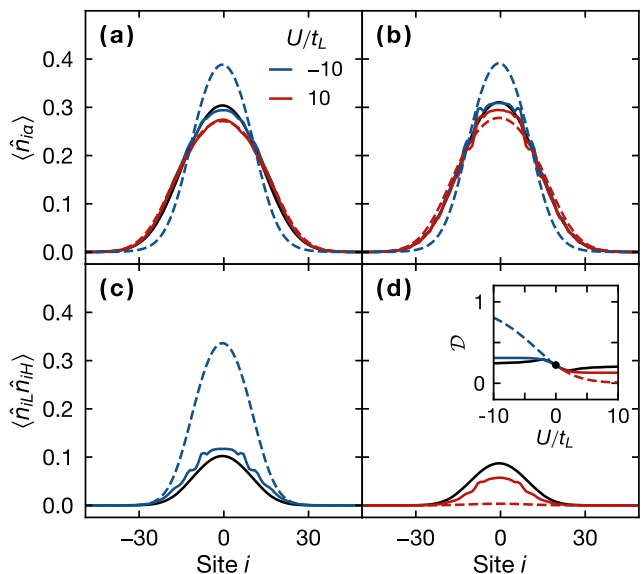


FIG. S9. Density profiles of (a) light atoms ($\alpha = L$), (b) heavy atoms ($\alpha = H$), and (c),(d) doublons at the end of our state preparation protocol from a numerical simulation for a single tube with $N_L = N_H = 10$ atoms. Solid colored lines correspond to the full state preparation protocol for $U/t_L = -10$ (attractive, blue) and 10 (repulsive, red) with typical experimental parameters, while the dashed lines represent the corresponding thermal state at the T_{eff} obtained from the local-density approximation and at finite interactions U/t_L . The black solid lines correspond to a non-interacting thermal state at temperature T_{eff} . In the inset of panel (d), we show the doublon fraction \mathcal{D} for variable interaction strength U/t_L and similar preparation protocols as in the main panels. Here, the solid black line corresponds to the non-interacting thermal state with an interaction quench $0 \rightarrow U/t_L$ and a subsequent hold time of $10\hbar/t_L$.

the initial state in the $\approx 7E_{\text{rec}}$ deep state-independent lattice, quench the hopping ratio $t_H/t_L = 1 \rightarrow 0.05$, apply the ramps for the confinement strength as well as hopping ratio, and subsequently turn on the interaction by ramping U/t_L to the desired value.

In Fig. S9, we show the density profiles $\langle \hat{n}_{i\alpha} \rangle$ of the light atoms ($\alpha = L$) and heavy atoms ($\alpha = H$) as well as the density of doublons $\langle \hat{n}_{iL}\hat{n}_{iH} \rangle$ after calculating the state preparation for an exemplary $N_L = N_H = 10$ tube with $U/t_L = -10$ and 10. Here, $\langle \hat{O} \rangle = \text{Tr}(\hat{\rho}\hat{O})$ denotes the expectation value of the corresponding operator \hat{O} . We compare the prepared state to a thermal equilibrium state at fixed temperature T_{eff} for strong interactions and for the non-interacting case. For this purpose, we choose the effective temperature of this state according to $T_{\text{eff}} = (\kappa_2/\kappa_1)T_{\text{init}} \simeq 2.3t_L/k_B$ where κ_1 (κ_2) is the trapping potential before (after) the state-independent optical lattice is ramped to the final depth (see Fig. S1). As shown in Figs. S9(a) and S9(b), the density profiles of light and heavy atoms for the prepared state are similar

to a thermal state at temperature T_{eff} on the repulsive side, while significant differences become visible for the strong attractive case. Furthermore, we put emphasis on the doublon density $\langle \hat{n}_{iL} \hat{n}_{iH} \rangle$ and relative fraction

$$\mathcal{D} = \frac{1}{N_L} \sum_i \langle \hat{n}_{iL} \hat{n}_{iH} \rangle. \quad (\text{S.20})$$

Due to the expected exponentially long lifetime [17] and suppressed mobility of doublons [18] ($\tau_{\mathcal{D}} \propto t^2/U$, for the mass-balanced case $t = t_L = t_H$), we expect the initial fraction of doublons to influence the transport properties in our system critically. Strikingly, the doublon fraction drastically deviates from the thermal state, which has a significantly higher (lower) value on the attractive (repulsive) side [see inset of Fig. S9(d)]. Our calculations suggest that the system does not thermalize during the state preparation and the resulting state is still close to a non-interacting state at T_{eff} . Moreover, the doublon fraction only weakly depends on the interaction strength, which is consistent with the symmetry between the attractive and repulsive side observed in the experiment [see Fig. 3].

2. Simulation of the transport measurement

Simulating the full dynamical response of our system even after displacing the trap minimum is generally limited by the rapidly growing operator space entanglement. To numerically access long enough times before truncation errors become significant, we do not perform the full preparation protocol but rather choose the non-interacting thermal state at T_{eff} as an approximate initial state and quench to the desired interaction strength. Comparing the density profiles and the doublon fraction verifies that this approximates the prepared state reasonably well (see black lines in Fig. S9). To further mitigate truncation errors due to growing entanglement, we only consider $N_L = N_H = 5$ atoms in this simulation. Fig. S10 shows the transport after displacing the trap minimum over a distance of $45d$ within $90\hbar/t_L$ for different interaction strength on the attractive side. The suppression of mobility with increasing $|U|/t_L$ becomes very clear and can be quantified by measuring the fraction of atoms on the right side of the system with $i \geq 0$, in analogy to the measurement of N_r/N in the experiment. The results for attractive and repulsive interactions are plotted in the inset of Fig. 3, and qualitatively agree with our experiment.

C. Many-body Stark localization

As discussed in the main text, harmonic confinement in the experiment leads to Stark localization of single-particle eigenstates with energies above the band edge

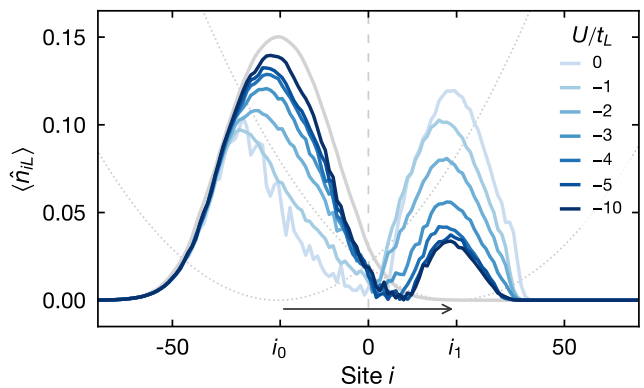


FIG. S10. Interaction-dependent transport of light atoms from a numerical simulation for a single tube of $N_L = N_H = 5$ atoms, transport distance $45d$, and transport duration of $90\hbar/t_L$. The solid gray line corresponds to the initial state located at the initial trap minimum i_0 and blue lines represent the evolved density profiles for different interaction strength after translating the trap minimum to i_1 . We indicate the initial and final harmonic confinement with dotted gray lines.

at $2t_L$. Hence, transport in the non-interacting case is strongly suppressed, especially for the heavy atoms, as these experience a much stronger effective confinement $\kappa/t_H \gg \kappa/t_L$ compared to the light atoms. For the interacting case, we expect some of these states to be delocalized through interactions [11, 19] already in the early time dynamics of our system. Nevertheless, many-body Stark localization [20] is still expected for strong enough trapping and has been studied, e. g. in Ref. [21] for the mass-balanced Fermi-Hubbard model (albeit relaxation at extremely late times cannot be fully ruled out). Here, we extend these studies to the mass-imbalanced case. To this end, we study the quench dynamics for an initial staggered product state

$$|\Psi_0\rangle = |L\ 0\ H\ 0\ \dots\rangle \quad (\text{S.21})$$

in a system of 64 sites for a typical hopping ratio of $t_H/t_L = 0.1$. We express the initial state as an exact MPS and calculate the time evolution with the TEBD algorithm.

Fig. S11 depicts the dynamics of the atomic densities for both species. The light atoms equilibrate on a time scale \hbar/t_L , and we observe relaxation for the given system size and confinement $\kappa/t_L = 2 \times 10^{-2}$. In contrast, relaxation of heavy atoms starts at a time scale \hbar/t_H and occurs in the center of the trap. Close to the edges of the system, the local gradient leads to a confinement of the heavy atoms on the simulated time scales. For the mass-balanced Fermi-Hubbard model, the local critical potential has been estimated as $\partial_i \mathcal{H} / \hat{n}_{i\alpha} = \kappa(i_{\text{crit}} - i_0) \simeq 2.8$ [21] which agrees well with our observations in the mass-imbalanced case. We therefore estimate that already at short times the heavy atoms are mobile over a

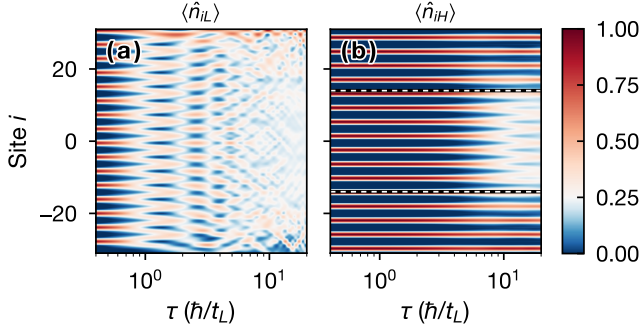


FIG. S11. Time-dependent quench dynamics of the atomic densities for an initial staggered state in a quarter filled system of size $l = 64$, shown for (a) light and (b) heavy atoms. The dashed lines in panel (b) indicate the boundary between localized and delocalized states. The Hubbard parameters are close to typical experimental values with $\kappa/t_L = 2 \times 10^{-2}$, $t_H/t_L = 0.1$, and $U/t_L = -1.0$. We note that the visible asymmetry on the edges of the system originates from the non-inversion-symmetric initial state.

central trap region of $2i_{\text{crit}} \approx 30$ lattice sites. Our simulations explicitly focus on weak interactions $U/t_L = -1.0$ to ensure that dynamical constraints arising from doublon physics and mass imbalance are weak, and we consequently only probe the influence of harmonic confinement on the mobility of the heavy atoms.

D. Relaxation dynamics of the mass-balanced case

In our experimentally realized Fermi-Hubbard model, mass imbalance between the two species induces strong dynamical constraints on the light atoms. Here, we briefly discuss the relaxation dynamics in the mass-balanced Fermi-Hubbard model, which we compare to the experimental data in the main text. To this end, we consider the Hamiltonian in Eq. (1) for the mass-balanced limit with species-independent hopping amplitude $t_L = t_H$, strong attractive interactions $U/t_L = -10$, and a small harmonic confinement $\kappa/t_L = 1 \times 10^{-2}$, approximately matching the experimental parameter. To estimate the relaxation time of a density modulation, we calculate the dynamical correlator

$$\mathcal{C}_{q\alpha}(\tau) = \langle \hat{n}_{q\alpha}^\dagger \hat{n}_{q\alpha}(\tau) \rangle, \quad (\text{S.22})$$

which measures the decay of an inhomogeneous density perturbation $\hat{n}_{q\alpha} = \sum_j e^{-iqj} \hat{n}_{j\alpha}$ for one species ($\alpha = L$). We simulate the Heisenberg time evolution of the operator \hat{n}_{qL} with the same method as discussed for the density matrix (see Section S.IIB), and subsequently measure the dynamical correlator by calculating the overlap with the initial purified operator. We note, that for the Heisenberg equation of motion $\partial_\tau \hat{O} = i[\hat{\mathcal{H}}, \hat{O}]$, the super-operator reads $\mathcal{L} = -\hat{\mathcal{H}} \otimes \mathbf{1} + \mathbf{1} \otimes \hat{\mathcal{H}}$.

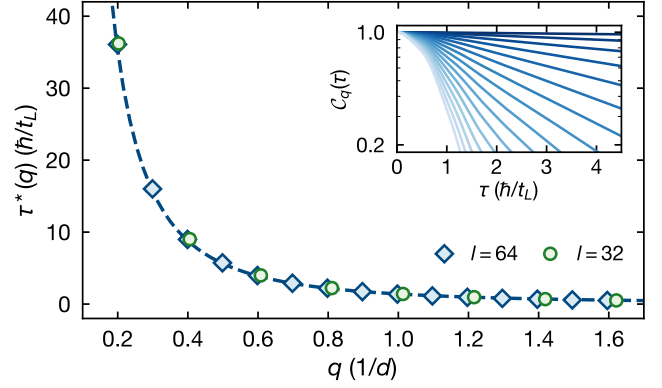


FIG. S12. Decay time $\tau^*(q)$ of density modulations in the mass-balanced Fermi-Hubbard model for different wavevectors $q = 2\pi/\lambda$ and system sizes l . We extract τ^* with an exponential fit of the short-time relaxation dynamics obtained from the dynamical correlator $\mathcal{C}_q(\tau)$, as shown in the inset for $l = 64$ with lighter (darker) blue solid lines corresponding to smaller (larger) λ . The dashed blue line corresponds to a fit of the $l = 64$ data to $\tau^*(q) = 1/(Dq^2)$ with the fit parameter $D \simeq 0.7d^2 t_L$.

From the exponential decay of the dynamical correlator at short times (see inset Fig. S12), we extract the decay constant $1/\tau^*$ for different excitation wavelengths. The decay time scales as $\tau^* = 1/(Dq^2)$ with $D \simeq 0.7d^2 t_L$ estimated from a fit of the short-time dynamics [see Fig. S12]. Note that at late times the integrable Hubbard model in the absence of a trapping potential is expected to show super-diffusive relaxation dynamics at half-filling or zero-magnetization and ballistic transport otherwise [22]. By contrast, here, we consider a finite trapping potential and study the short time relaxation dynamics, which possesses the same scaling as diffusive relaxation. Varying the system size does not change our result significantly, which indicates that finite-size effects can be neglected. From these considerations, we can estimate the typical decay time of the mass-balanced case for the experimentally relevant initial conditions, where the atomic cloud is displaced by $20d$. Hence, the corresponding wavevector is $q \sim \pi/(20d) \simeq 0.16/d$ yielding an estimated decay time of $\tau^* \simeq 58\hbar/t_L$, which is significantly faster than the ones observed for the mass-imbalanced case in the main text.

E. Time scales

It has been shown that strong mass imbalance in small translational-invariant ($\kappa = 0$) systems leads to an ergodic regime of extremely slow equilibration [23]. For the delocalized atoms in the center of the trap, we expect the dynamics to be close to this $\kappa \rightarrow 0$ limit. This suggests that our finite-size experimental system with large mass

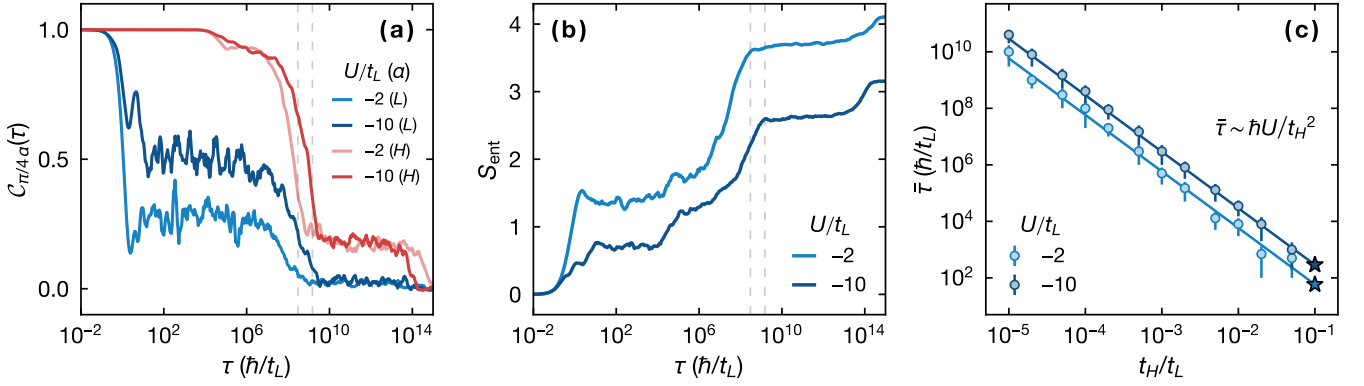


FIG. S13. Extraction of time scales for large mass imbalance. (a) Decay of a long-wavelength excitation and (b) growth of entanglement entropy for initial product states evaluated for a translational-invariant, periodic system of size $l = 8$ for $N_L = N_H = 4$ atoms. We consider the interactions strengths $U/t_L = -2$ and -10 for the extreme mass-imbalanced case of $t_H/t_L = 5 \times 10^{-5}$ to exemplify the different time scales. (c) Time scale $\bar{\tau} = C \times \hbar U/t_H^2$ corresponding to the onset of the final metastable regime [dashed lines in panels (a) and (b)]. Here, the constant C is extracted from a fit shown as solid lines. We indicate the experimentally relevant values for $t_H/t_L = 0.1$ with star-shaped markers.

imbalance will feature similar physics. To study the involved time scales, we turn to very large mass imbalance and long evolution times. For this purpose, we perform exact diagonalization of the translational-invariant model with the Hamiltonian in Eq. (1) taking the form,

$$\hat{\mathcal{H}}' = - \sum_{i,\alpha \in \{L,H\}} t_\alpha \left[\hat{c}_{i\alpha}^\dagger \hat{c}_{(i+1)\alpha} + \text{h.c.} \right] + U \sum_i \hat{n}_{iL} \hat{n}_{iH}, \quad (\text{S.23})$$

subject to periodic boundary conditions, $\hat{c}_{l\alpha}^\dagger = \hat{c}_{0\alpha}^\dagger$, for a system of size $l = 8$ at half filling $N_L = N_H = 4$.

The decay of long-wavelength modulations is shown in Fig. S13(a) for $t_H/t_L = 5 \times 10^{-5}$ and indicates the existence of distinct time scales governing the dynamics [also see Fig. 1(c)]. These time scales also become apparent in the entanglement dynamics corresponding to plateau-like features of very slow entanglement growth [see Fig. S13(b)]. Here, we compute the half-chain entanglement entropy for random initial product states, averaging the results of 20 states. After initial relaxation of the light particles on the time scale $\sim \hbar/t_L$ the dynamics stagnate, and the entanglement entropy stays nearly constant up to time $\sim \hbar/t_H$. Following further relaxation and an increase of the entanglement entropy, the system enters a new metastable regime at time scale $\sim \hbar U/t_H^2$ [dashed lines in Figs. S13(a) and S13(b)]. This regime features exponentially slow decay of non-equilibrium states [23], and we observe an accordingly slow growth of entanglement entropy. Although the phenomenology shows similarities to a dynamical type of many-body localization, the system is still ergodic, and density perturbations eventually decay. From our exact diagonalization data, we extract the time scale $\bar{\tau} = C \times \hbar |U|/t_H^2$ for the onset of this regime and estimate

$C = 0.29(3)$ from a fit [see Fig. S13(c)]. For our experimental case, this results in $\bar{\tau} \simeq 270(28)_{\text{fit}}(51)_{\text{exp.}} \hbar/t_L$ with $t_H/t_L = 0.102(6)$ and $U/t_L = -9.7(7)$ [see Fig. 4(b) and Table S1]. We note that for increasing t_H/t_L and increasing system size, the features separating different regimes become less pronounced. Nevertheless, our calculations suggest that we are able to reach the final regime of metastability within the experimentally accessible times.

* n.darkwahoppong@lmu.de

- [1] O. Bettermann, N. Darkwah Oppong, G. Pasqualetti, L. Riegger, I. Bloch, and S. Fölling, Clock-line photoassociation of strongly bound dimers in a magic-wavelength lattice, [arXiv:2003.10599](https://arxiv.org/abs/2003.10599).
- [2] M. Kitagawa, K. Enomoto, K. Kasa, Y. Takahashi, R. Ciuryło, P. Naidon, and P. S. Julienne, Two-color photoassociation spectroscopy of ytterbium atoms and the precise determinations of s -wave scattering lengths, *Phys. Rev. A* **77**, 012719 (2008).
- [3] M. Köhl, Thermometry of fermionic atoms in an optical lattice, *Phys. Rev. A* **73**, 031601 (2006).
- [4] N. Darkwah Oppong, L. Riegger, O. Bettermann, M. Höfer, J. Levinsen, M. M. Parish, I. Bloch, and S. Fölling, Observation of Coherent Multiorbital Polarons in a Two-Dimensional Fermi Gas, *Phys. Rev. Lett.* **122**, 193604 (2019).
- [5] I. Bloch, J. Dalibard, and W. Zwerger, Many-body physics with ultracold gases, *Rev. Mod. Phys.* **80**, 885 (2008).
- [6] S. Friebe, C. D'Andrea, J. Walz, M. Weitz, and T. W. Hänsch, CO₂-laser optical lattice with cold rubidium atoms, *Phys. Rev. A* **57**, R20 (1998).
- [7] C. Chin, R. Grimm, P. Julienne, and E. Tiesinga, Feshbach resonances in ultracold gases, *Rev. Mod. Phys.* **82**,

- 1225 (2010).
- [8] E. K. Laird, Z.-Y. Shi, M. M. Parish, and J. Levinsen, Frustrated orbital Feshbach resonances in a Fermi gas, *Phys. Rev. A* **101**, 022707 (2020).
- [9] L. Riegger, N. Darkwah Oppong, M. Höfer, D. R. Fernandes, I. Bloch, and S. Fölling, Localized Magnetic Moments with Tunable Spin Exchange in a Gas of Ultracold Fermions, *Phys. Rev. Lett.* **120**, 143601 (2018).
- [10] U. Schneider, L. Hacker Müller, J. P. Ronzheimer, S. Will, S. Braun, T. Best, I. Bloch, E. Demler, S. Mandt, D. Rasch, and A. Rosch, Fermionic transport and out-of-equilibrium dynamics in a homogeneous Hubbard model with ultracold atoms, *Nat. Phys.* **8**, 213 (2012).
- [11] N. Strohmaier, Y. Takasu, K. Günter, R. Jördens, M. Köhl, H. Moritz, and T. Esslinger, Interaction-Controlled Transport of an Ultracold Fermi Gas, *Phys. Rev. Lett.* **99**, 220601 (2007).
- [12] F. Verstraete, J. J. García-Ripoll, and J. I. Cirac, Matrix Product Density Operators: Simulation of Finite-Temperature and Dissipative Systems, *Phys. Rev. Lett.* **93**, 207204 (2004).
- [13] M. Zwolak and G. Vidal, Mixed-State Dynamics in One-Dimensional Quantum Lattice Systems: A Time-Dependent Superoperator Renormalization Algorithm, *Phys. Rev. Lett.* **93**, 207205 (2004).
- [14] J. Hauschild and F. Pollmann, Efficient numerical simulations with Tensor Networks: Tensor Network Python (TeNPy), *SciPost Phys. Lect. Notes* , 5 (2018).
- [15] S. Paeckel, T. Köhler, A. Swoboda, S. R. Manmana, U. Schollwöck, and C. Hubig, Time-Evolution Methods for Matrix-Product States, *Ann. Phys. (N. Y.)* **411**, 167998 (2019).
- [16] G. Vidal, Efficient Simulation of One-Dimensional Quantum Many-Body Systems, *Phys. Rev. Lett.* **93**, 040502 (2004).
- [17] R. Sensarma, D. Pekker, E. Altman, E. Demler, N. Strohmaier, D. Greif, R. Jördens, L. Tarruell, H. Moritz, and T. Esslinger, Lifetime of Double Occupancies in the Fermi-Hubbard Model, *Phys. Rev. B* **82**, 224302 (2010).
- [18] A. Auerbach, *Interacting Electrons and Quantum Magnetism* (Springer, New York, 1994).
- [19] H. Ott, E. de Mirandes, F. Ferlino, G. Roati, G. Modugno, and M. Inguscio, Collisionally Induced Transport in Periodic Potentials, *Phys. Rev. Lett.* **92**, 160601 (2004).
- [20] M. Schulz, C. A. Hooley, R. Moessner, and F. Pollmann, Stark Many-Body Localization, *Phys. Rev. Lett.* **122**, 040606 (2019).
- [21] T. Chanda, R. Yao, and J. Zakrzewski, Coexistence of localized and extended phases: Many-body localization in a harmonic trap, *Phys. Rev. Research* **2**, 032039(R) (2020).
- [22] M. Fava, B. Ware, S. Gopalakrishnan, R. Vasseur, and S. A. Parameswaran, Spin crossovers and superdiffusion in the one-dimensional Hubbard model, *Phys. Rev. B* **102**, 115121 (2020).
- [23] N. Y. Yao, C. R. Laumann, J. I. Cirac, M. D. Lukin, and J. E. Moore, Quasi-Many-Body Localization in Translation-Invariant Systems, *Phys. Rev. Lett.* **117**, 240601 (2016).